1.0

1.1

1.25   1.4   1.6

4.5
5.0
5.5

2.8   2.5

3.2   2.2

3.6

4.0   2.0

1.8

MICROCOPY RESOLUTION TEST CHART
NATIONAL BUREAU OF STANDARDS-1963-A

LEVEL 12

RADC-TR-80-11
Final Technical Report
April 1980

DEVELOPMENT OF 1.0- TO 1.4-μm HETEROJUNCTION LEDs

RCA Laboratories

G. H. Olsen
M. Ettenberg
C. J. Nuese
D. Botez

DTIC
ELECTE
JUL 1 1980
C

This report has been reviewed by the RADC Public Affairs Office (PA) and is releasable to the National Technical Information Service (NTIS). At NTIS it will be releasable to the general public, including foreign nations.

RADC-TR-80-110 has been reviewed and is approved for publication.

APPROVED:

D. EIRUG DAVIES
Project Engineer

APPROVED:

CLARENCE D. TURNER
Acting Director
Solid State Sciences Division

FOR THE COMMANDER:

JOHN P. HUSS
Acting Chief, Plans Office

REPORT DOCUMENTATION PAGE		READ INSTRUCTIONS BEFORE COMPLETING FORM
1. REPORT NUMBER RADC-TR-80-110	2. GOVT ACCESSION NO. AD-A086 082	3. RECIPIENT'S CATALOG NUMBER
4. TITLE (and Subtitle) DEVELOPMENT OF 1.0 TO 1.4-μm HETEROJUNCTION LEDs		5. TYPE OF REPORT & PERIOD COVERED Final Technical Report 17 Apr 78 — 16 Mar 79
		6. PERFORMING ORG. REPORT NUMBER PRRL-79-CR-18
7. AUTHOR(s) G. H. Olsen C. J. Nuese M. Ettenberg D. Botez		8. CONTRACT OR GRANT NUMBER(s) F19628-78-C-0105
9. PERFORMING ORGANIZATION NAME AND ADDRESS RCA Laboratories Princeton NJ 08540		10. PROGRAM ELEMENT, PROJECT, TASK AREA & WORK UNIT NUMBERS 62702F 46001922
11. CONTROLLING OFFICE NAME AND ADDRESS Deputy for Electronic Technology (RADC/ESO) Hanscom AFB MA 01731		12. REPORT DATE April 1980
		13. NUMBER OF PAGES 64
14. MONITORING AGENCY NAME & ADDRESS(if different from Controlling Office) Same		15. SECURITY CLASS. (of this report) UNCLASSIFIED
		15a. DECLASSIFICATION DOWNGRADING SCHEDULE N/A

16. DISTRIBUTION STATEMENT (of this Report)

Approved for public release; distribution unlimited.

17. DISTRIBUTION STATEMENT (of the abstract entered in Block 20, if different from Report)

Same

18. SUPPLEMENTARY NOTES
RADC Project Engineer: D. Eirug Davies (RADC/ESO)

19. KEY WORDS (Continue on reverse side if necessary and identify by block number)
Edge-emitting LEDs
Surface-emitting LEDs
Vapor-phase epitaxy
Fiber coupling

20. ABSTRACT (Continue on reverse side if necessary and identify by block number)
Both VPE and LPE InGaAsP/InP edge-and surface-emitting LEDs have been fabricated and tested under the present contract. Table 1 contains a summary of the results. Although the surface emitter provides greater total power, its halfwidth is considerably larger than that of the edge emitter. This increases pulse dispersion and reduces the amount of power that can be coupled into an optical fiber.
(Continued)

DD FORM 1473   EDITION OF 1 NOV 65 IS OBSOLETE
1 JAN 73

299000

The experimental conditions for the vapor-phase growth of InGaAsP and InP alloy are described. Detailed growth procedures are specified and plots of alloy composition, bandgap, lattice parameter and doping levels vs growth parameters are included.

Modulation rates close to 100 MHz have been measured for 1.27-μm edge-emitting LEDs. Fall times on the order of 10 ns for (90 to 10% response) also have been obtained.

Over fifty edge-emitting VPE 1.27-μm heterojunction LEDs have been fabricated from numerous wafers. External power efficiencies >0.3% were routinely measured, with maximum efficiencies on the order of 0.7% (from one edge). Wafer-to-wafer reproducibility of power efficiencies has now been demonstrated with both the LPE and VPE growth techniques.

Over 100 μW of optical power have been coupled into a 50-μm core 0.2-NA graded-index fiber using a VPE 1.27-μm LED driven at 200 mA.

Experiments with AlGaAs have shown that the optical power coupled into a fiber is higher for edge-emitting LEDs than for surface-emitting LEDs, when the numerical aperture is less than 0.4 and data rates exceed 25 Mbit/s.

TABLE OF CONTENTS

LIST OF ILLUSTRATIONS

iv

LIST OF ILLUSTRATIONS (Continued)

LIST OF TABLES

EVALUATION

This is the final report on the contract. The objective of the research was to optimize InGaAsP light emitting diodes for fiber optic applications. Maximum external power efficiencies were on the order of 0.7% (from one edge) and over 100 μW could be coupled into 50 μm core 0.2 graded index fibers. Though greater total power was obtained with surface emitters, better coupling favored edge emitters in low numerical aperture fibers at data rates exceeding 25 MB/sec. This work has applications to TPO R3B.

D. EIRUG DAVIES
Project Engineer

I. SUMMARY

Both VPE and LPE InGaAsP/InP edge- and surface-emitting LEDs have been fabricated and tested under the present contract. The following contains a summary of results. Although the surface emitter provides greater total power its half-width is somewhat larger than that of the edge emitter. This increases pulse dispersion and reduces the amount of power that can be coupled into an optical fiber.

LPE and VPE: Edge vs Surface Emission

Type	Emission	$\lambda(\mu m)$	$\Delta\lambda(\mathring{A})$	$(\eta_{power}$ (%)
VPE Ternary	Edge	1.06	500	0.45
VPE Quaternary	Edge	1.12	500	0.50
VPE Quaternary	Edge	1.27	700	0.61
VPE Quaternary	Surface	1.27	1350	0.70
LPE Quaternary	Edge	1.32	750	0.7
LPE Quaternary	Surface	1.32	1250	1.7

Modulation rates of 70 to 100 MHz (3-dB optical) have been measured for 1.27-μm edge-emitting LEDs. Fall times on the order of 10 ns (90 to 10% response) also have been obtained.

Over fifty edge-emitting VPE 1.27-μm heterojunction LEDs have been fabricated from numerous wafers. External power efficiencies $\geq 0.3\%$ were routinely measured, with maximum efficiencies on the order of 0.7% (from one edge). Wafer-to-wafer reproducibility of power efficiencies has now been demonstrated with both the LPE and VPE growth techniques.

Over 100 μW of optical power have been coupled into a 50-μm core, 0.2-NA (numerical aperture) graded-index fiber using a VPE 1.27-μm LED driven at 200 mA.

Experiments with AlGaAs have shown that the optical power coupled into a fiber is higher for edge-emitting LEDs than for surface-emitting LEDs, when the numerical aperture is less than 0.4 and data rates exceed 25 Mbit/s.

1

The experimental conditions for the vapor-phase of InGaAsP and InP alloy are described. Detailed growth procedures are specified and plots of alloy composition, bandgap, lattice parameter and doping levels vs growth parameters are included.

II. INTRODUCTION

To date, most fiber-optic sources have been AlGaAs heterojunction lasers and LEDs emitting between 0.8 and 0.9 µm, with Si PIN or avalanche diodes serving as photodetectors. However, silica fiber-optic systems have several advantages at wavelengths greater than 1.0 µm.

First, the optical losses of high-purity silica fibers are about four times lower at 1.1 µm than at 0.8 µm [1]. As silica fibers are made purer, so that the OH vibrational overtones are reduced, the losses of silica fibers approach that due to Rayleigh scattering, which has a wavelength dependence of the form λ^{-4}. The reduced fiber losses at long wavelengths are particularly attractive for long-distance communication systems, where repeater spacing can be increased substantially.

A second major advantage lies in the fact that the material dispersion of silica fibers decreases with increasing wavelength [2]. This is due to the wavelength dependence of the refractive index, which predicts that material dispersion will approach zero at a wavelength near 1.27 µm. The spread of a light pulse propagating along a fiber is proportional to the product of the material dispersion of the fiber and the spectral pulse width. Since the spectral width for LEDs is on the order of several hundred angstroms (several tens of nanometers), pulse spreading can be as large as 3 ns (per kilometer of fiber) at 0.82 µm, but is reduced to less than 1 ns at 1.1 µm.

Finally, experiments with certain silica fibers [3] indicate considerably more resistance to neutron and gamma radiation at 1.1 µm than at shorter wavelengths. This factor might be important for military and/or space applications.

Concerning sources for long-wavelength fiber systems, both LEDs and lasers are being seriously considered. For many applications, an LED offers real advantages. For example, an LED is typically a simpler structure than a laser, with dimensions that are not as critical. LEDs also typically operate at lower current densities than lasers, and therefore exhibit slower degradation rates

1. N. Horiguchi, Electron. Lett. 12, 310 (1976).
2. D. N. Tayne and W. A. Gambling, Electron. Lett. 11, 176 (1975).
3. C. J. Nuese and G. H. Olsen, Appl. Phys. Lett. 26, 528 (1975).

than lasers. The lack of a threshold current for an LED also reduces the effect of degradation on device efficiency, and considerably simplifies driving and modulating circuitry.

Two types of LEDs have been developed for fiber-optic applications: edge-emitting diodes and surface-emitting diodes. The surface emitter generally provides larger total radiated power, but its emission pattern is close to Lambertian (very broad), making coupling to fibers with low numerical apertures inefficient. The edge emitter has reduced total emission, but a higher radiance, with a narrower (beam-like) emission pattern. This is desirable for coupling diode radiation into fibers with low numerical apertures.

The program we undertook involved the preparation and evaluation of fiber-compatible sources of both the edge-emitter and the surface-emitter types by both liquid-phase and vapor-phase growth techniques. The materials used were: (i) InGaAs, a direct-bandgap ternary alloy with well-understood electronic properties for which highly developed preparative techniques are available at RCA Laboratories; (ii) InGaAsP, a direct-bandgap quaternary alloy that can be directly lattice-matched to InP substrates. The objective of the program was to develop and evaluate LED sources from these two materials, to measure their output, speed- and fiber-coupling efficiency, and to compare edge- and surface-emitting LEDs.

III. DEVICE SYNTHESIS - EPITAXIAL GROWTH TECHNIQUES

The ternary and quaternary structures discussed throughout this report were prepared by vapor-phase and liquid-phase epitaxial growth techniques pioneered and developed at RCA Laboratories, Princeton, N.J. The basic principles involved in the RCA vapor-phase and liquid-phase growth techniques are briefly introduced in this section. In subsequent sections, the application of these growth technologies to the preparation of long-wavelength LEDs is treated in detail.

A. VAPOR-PHASE EPITAXY

The RCA vapor-phase method has been applied to the epitaxial deposition of a wide variety of III-V compounds and alloys [4,5]. This method not only permits these materials to be prepared in a state of high purity and homogeneity, but also allows precise and independent control of layer thickness, alloy composition, and both n- and p-type doping. As a result, multilayer structures can be incorporated into the crystal entirely during the growth process. This has already led to the fabrication of several outstanding devices, including LEDs, transistors, varactor diodes, Gunn-effect devices, 4-layer switching devices, and homojunction and heterojunction laser diodes.

The RCA vapor-growth method involves an epitaxial deposition in a flow system, and has the unique feature that the primary source chemicals are predominantly gaseous at room temperature. This avoids fluctuations related to the exponential temperature dependence of the reactant vapors associated with solids and liquids, and, thereby, ensures a high degree of crystal homogeneity. In addition, the use of gases provides a high degree of flexibility for controlling alloy composition or dopant impurity levels, since the reactant concentrations are accurately established by precision flow meters and valves. This is particularly desirable for the preparation of heterojunction structures, since the composition of the constituent alloys must be accurately controlled to prevent the introduction of lattice-misfit dislocations at the heteroepitaxial interfaces.

The apparatus used to prepare binary, ternary, or quaternary alloys of the elements In, Ga, As, and P is shown schematically in Fig. 1. The use of separate

4.   J. J. Tietjen and J. A. Amick, J. Electrochem. Soc. 113, 724 (1966).
5.   G. H. Olsen and M. Ettenberg, Crystal Growth: Theory and Techniques, edited by C. Goodman (Plenum, New York, 1978) Vol. II.
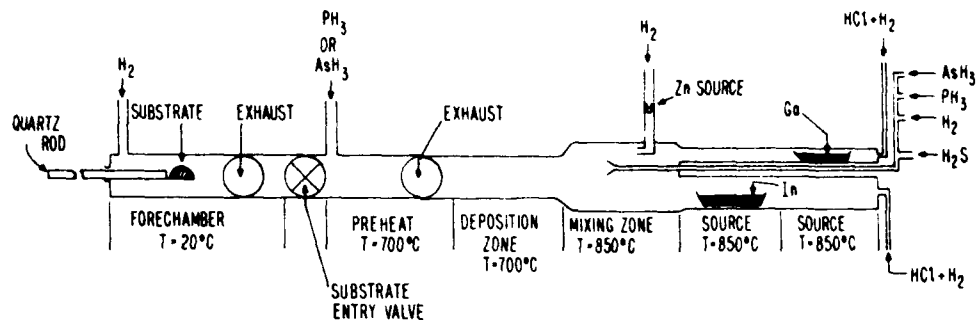
Figure 1. Sketch of RCA vapor-growth system.

source zones for In and Ga allows independent control of the temperature and the HCl concentration at each metal source. The HCl reacts with the hot metals forming their monochlorides, which are gaseous. These are carried in hydrogen into the mixing zone, where they combine but do not react with gaseous arsine or phosphine, the sources of arsenic and phosphorus. Mass-flow control valves are used on all input lines of the reactant species to ensure stable flow rates.

A typical growth process begins by inserting the substrate into the fore-chamber while flows of HCl are established over the metals and the Group V hydride gas(es) is (are) introduced. A photograph of the quartz-growth tube is shown in Fig. 2. Note how the InCl and GaCl tubes are directed against the gas flow to promote mixing. Composition is controlled by adjusting one of the alloying species (e.g., HCl over the In for $In_xGa_{1-x}P$). When all flows have been established, the substrate is preheated and then inserted into the deposition zone, which is the coolest region in the growth system. The reduced temperature allows the reaction between the chlorides, arsenic, phosphorus, and hydrogen to deposit the desired ternary or quaternary alloy as an epitaxial film and to form HCl as a gaseous by-product. Growth is terminated by withdrawing the wafer to the forechamber where it cools quickly ($\sim$10 min) to room temperature in a hydrogen atmosphere.

The provisions for n- and p-type doping using H_2S and Zn, respectively, are also shown in Fig. 1. For p-n junction formation, the dopants are introduced sequentially during vapor deposition.

Experimentally derived conditions for the VPE growth of InGaAsP alloys (wth bandgaps near 1.3 μm) on InP substrates are shown in Figs. 3 through 6.

6
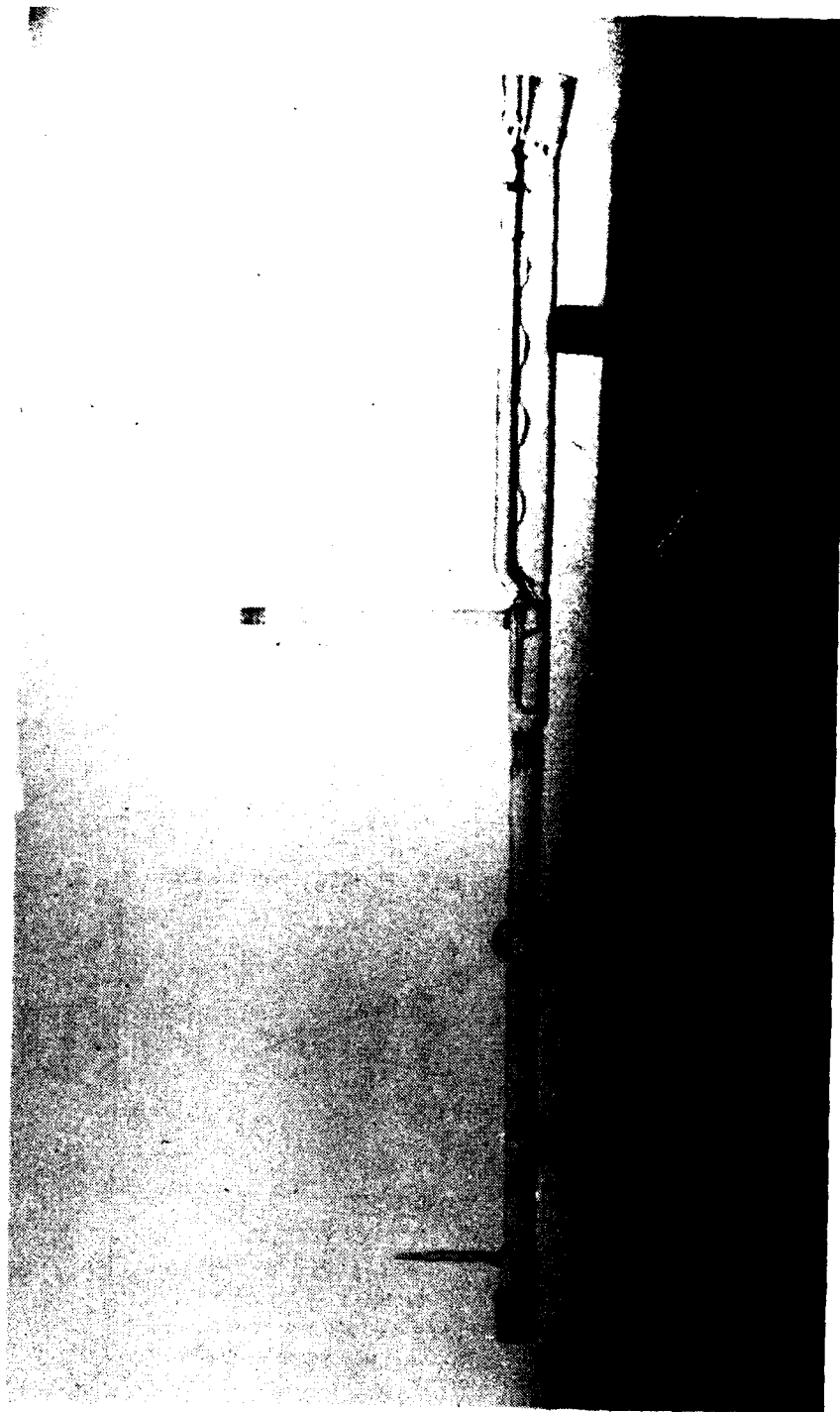
Figure 2. Photograph of 30-mm (I.D.) quartz-growth tube for VPE system.

7
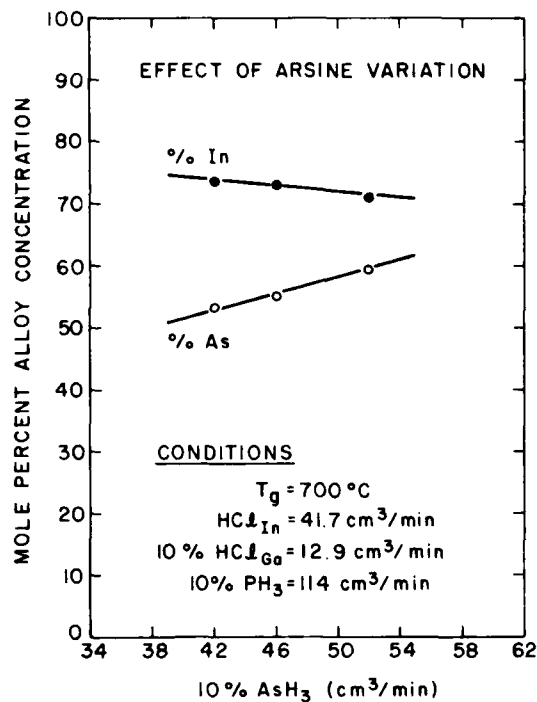
Figure 3. Effect of arsine flow on InGaAsP composition.
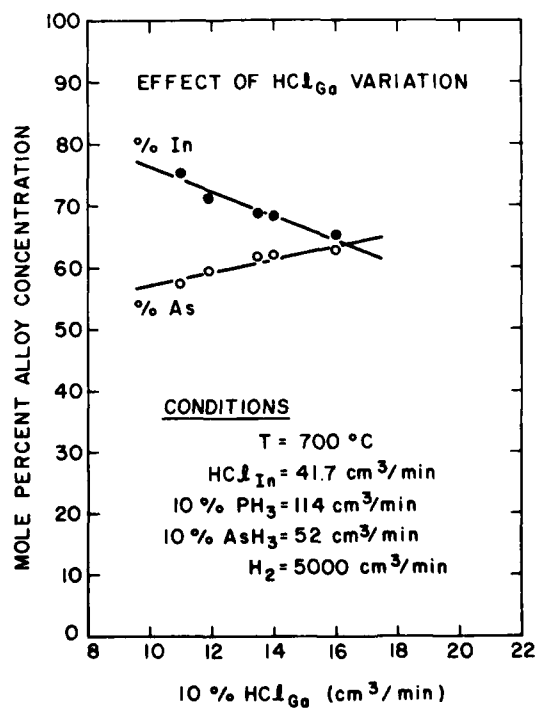
Figure 4. Effect of HCl$_{Ga}$ flow on InGaAsP composition.

8
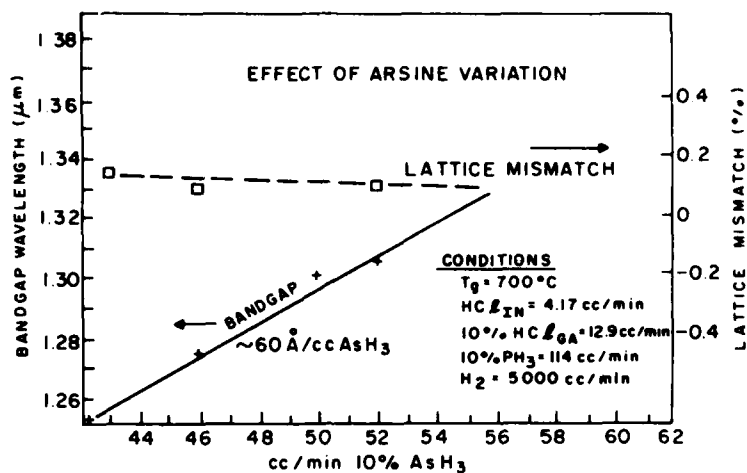
Figure 5. Effect of arsine flow on bandgap and lattice
parameter of InGaAsP.
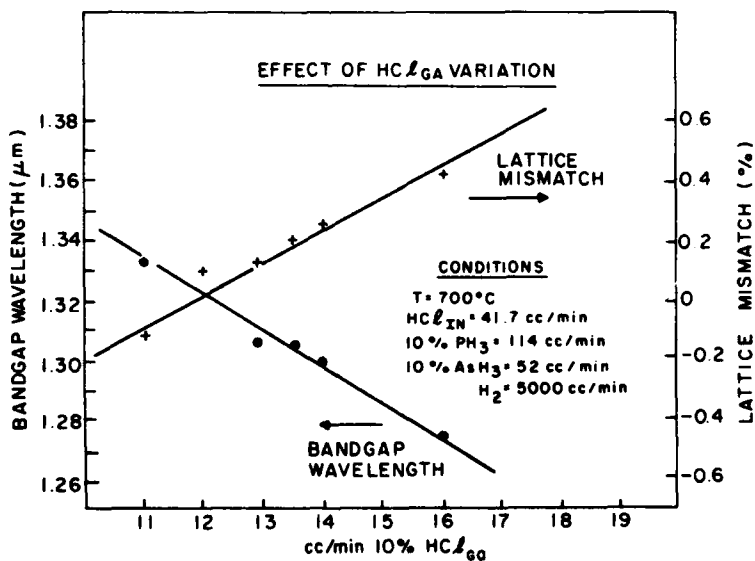
Figure 6. Effect of HCl_{Ga} flow on bandgap and lattice
parameter of InGaAsP.

9

Figure 3 shows how the alloy concentration varies with arsine flow (other conditions held constant) while Fig. 4 denotes the variation with HCl_{Ga}. Figures 5 and 6 depict the lattice parameter and bandgap variations with these same flows. The actual gas flows used for InGaAsP alloys with $\lambda \sim 1.3$ μm are listed on these figures. InP is grown by simply turning off the AsH_3 and HCl_{Ga}. Note that the lattice parameter varies very little with AsH_3 flow. Thus, if conditions for a lattice-matched alloy were known and only the band-gap were to be changed, only the arsine should be changed. On the other hand, if an alloy were lattice-mismatched to the InP substrate, it could most easily be corrected by changing the HCl_{Ga} flow in order to reestablish the lattice match, and then fine-tuning the wavelength with the arsine flow.

Figure 7 shows the effect of phosphine variation on the bandgap and lattice parameter of some short wavelength InGaAsP alloys deposited on GaAs substrates. Here, growth conditions were obtained by stating with known flow, settings for the growth of InGaAs and InGaP alloys. As the phosphine flow is increased, the bandgap and lattice parameters are seen to asymptotically approach the values for $In_{0.5}Ga_{0.5}P$.

The variation in In and P composition with growth temperature is plotted in Fig. 8. Note that both values decrease at a rate of mole % per °C as the temperature is increased. This is consistent with observations on ternary alloys as explained in Section IV.

The variation in N- and P-type doping level with zinc temperature and hydrogen sulfide flow is shown in Figs. 9 and 10 for both InP and InGaAsP ($\lambda \sim 1.3$ μm). The acceptor concentration in both alloys varies steeply with zinc temperature which must be carefully controlled.

B. LIQUID-PHASE EPITAXY

Beginning with the preparation of Ge for tunnel diodes [6], the deposition of semiconductor films by liquid-phase epitaxy (LPE) has rapidly been developed into a generally useful technique for the preparation of films of many III-V

6. H. Nelson, RCA Rev. 24, 603 (1963).
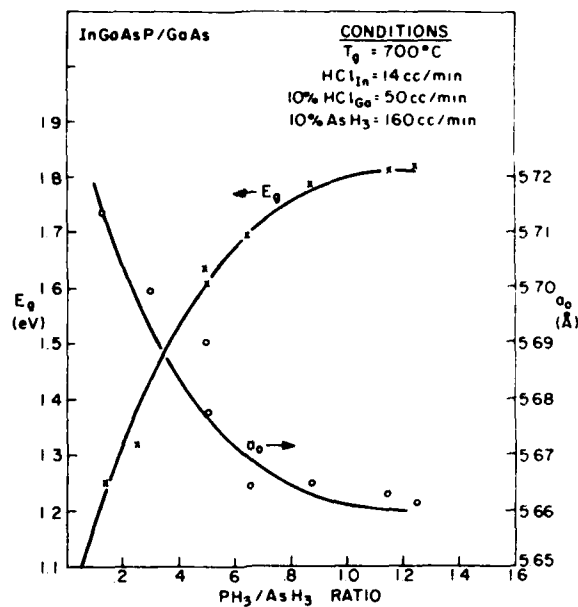
Figure 7. Composition of VPE InGaAsP alloys vs growth temperature.
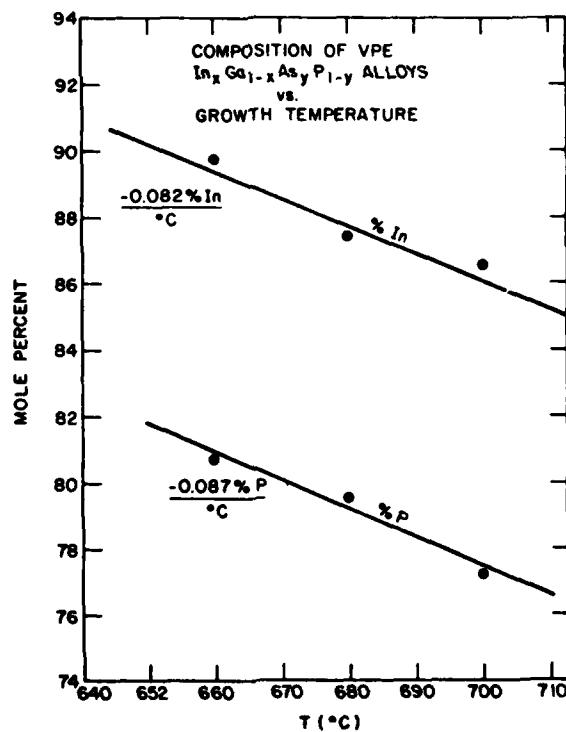
Figure 8. Effect of $PH_3/As\ H_3$ ratio on bandgap and lattice
parameter of InGaAsP alloys grown on GaAs substrates.

ZINC DOPING OF InP AND
QUATERNARY WITH ZINC TEMPERATURE
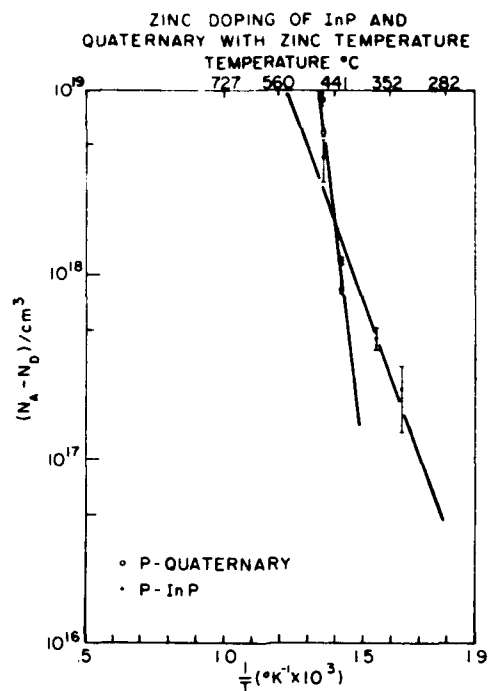
Figure 9. Net acceptor concentration in InGaAsP alloys vs
zinc temperature.
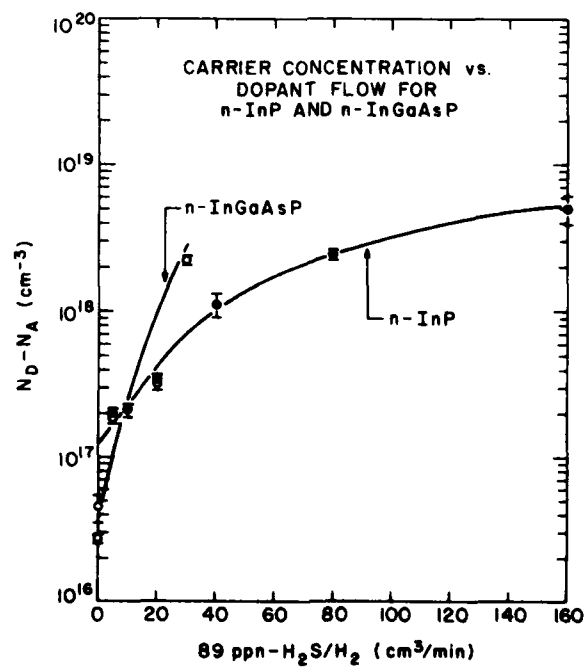
Figure 10. Net donor concentration in InGaAsP alloys vs
H_2S flow.

compounds [7]. Basically, LPE involves the precipitation of material from a cooling solution onto an underlying substrate. The solution and the substrate are kept apart in the growth apparatus and the solution is saturated with the growth material until the desired growth temperature is reached. The solution is then brought into contact with the substrate surface and allowed to cool at a rate and a time interval that are appropriate for the generation of the desired layer. When the substrate is single crystalline, and the lattice constant of the precipitation material is the same or nearly the same as that of the substrate, the precipitating material forms a layer on the substrate which is an extension of the single-crystal body of the substrate.

The RCA liquid-phase growth system uses a multibin boat, an important innovation in LPE technology because it allows sequential deposition of several semiconductor layers during one growth cycle. The graphite boat used in the first model of this apparatus is shown in Fig. 11. This graphite boat is provided with three reservoirs and a movable graphite slide, the upper surface of which constitues the bottoms of the reservoirs. The substrate is placed in a recessed area of the slide, and prior to growth is outside the reservoirs. The graphite boat, with the bins filled with appropriate In or Ga solutions, is inserted into a quartz furnace tube. A long rod fitted into a sleeve at the end of the furnace is used to slide the substrate sequentially into the bottom of the various reservoirs. In this manner, by a choice of appropriate solutions and temperature schedules, different types of films can be deposited sequentially onto the substrate surface.

Present boats have more bins and are considerably more sophisticated than this simple one; however, the procedures used are similar. With the RCA liquid-phase apparatus, ternary alloys of AlGaAs and quaternary/binary structures of InGaAsP/InP have been successfully prepared.

7. H. F. Lockwood and M. Ettenberg, U.S. Patent No. 3 741 825 (1973).
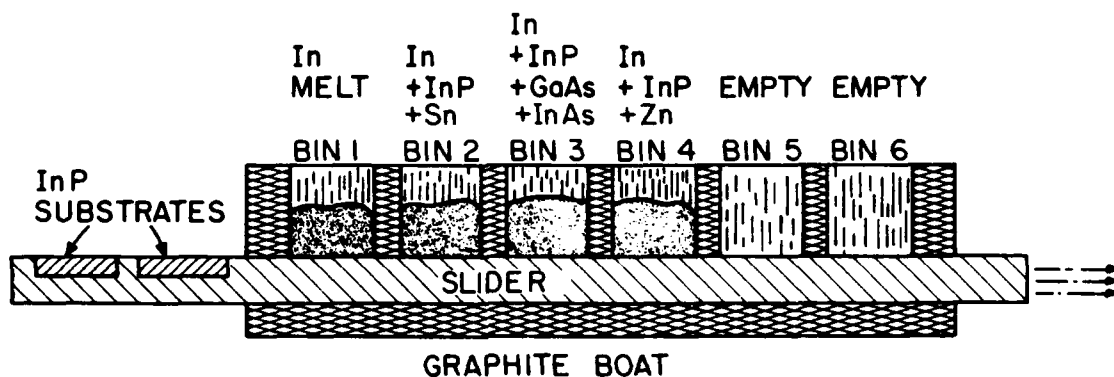
Figure 11(a). Sketch of RCA liquid-phase-epitaxy graphite boat.
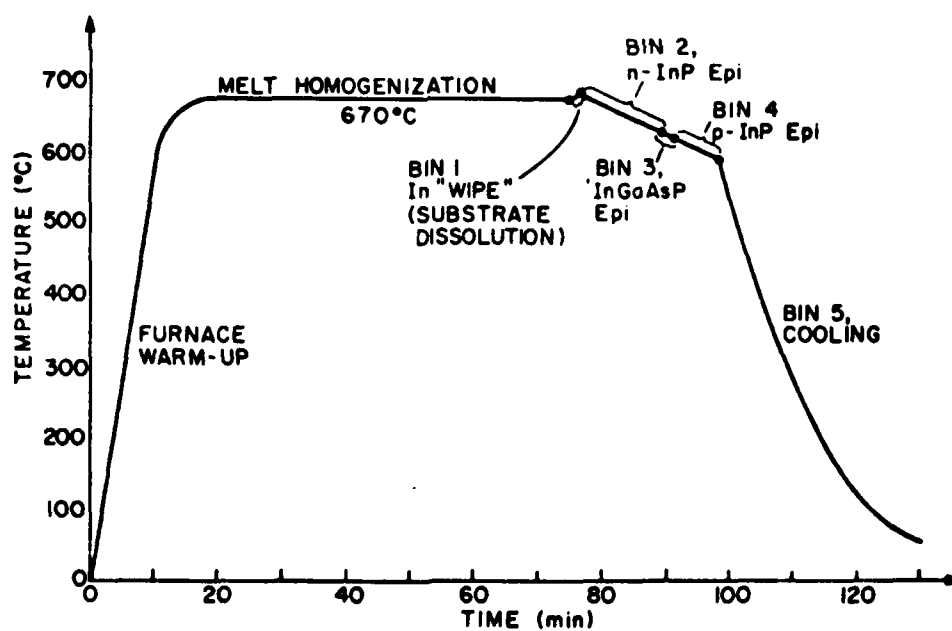
Figure 11(b). Graph depicting epitaxial growth process.

IV. DEVICE STRUCTURES - MATERIAL SELECTION

Two possible materials systems for the fabrication of 1.1- to 1.4-μm heterojunction LEDs are: (a) the InGaAs/InGaP ternary-ternary system, and (b) the InGaAsP/InP quaternary-binary system. The ternary system is well established at RCA, and 1.06-μm double-heterojunction lasers that exhibit the best device properties yet reported have been prepared with this system. The InGaAsP quaternary system, while only recently explored, offers several advantages over the ternary system, and might provide improved device yield and reliability. Each of these materials systems will be explored under the program proposed here, and is described more fully below.

A. TERNARY InGaAs/InGaP STRUCTURES

The vapor-grown ternary heterojunction structures prepared at RCA take advantage of the large variation of the lattice parameter of the $In_xGa_{1-x}P$ alloy system ($a_o = 5.45$ Å for GaP; $a_o = 5.87$ Å for InP). This lattice-parameter range allows particular alloys of $In_yGa_{1-y}P$ to be deposited heteroepitaxially onto layers of $In_xGa_{1-x}As$ ($x \lesssim 0.53$) so that the two semiconductor layers are very closely lattice-matched. In this way, dislocation densities at the interfaces are reduced, and p-n junctions placed at or in close proximity to the interfaces can be of high quality. A schematic representation of the lattice parameter values of the two alloy systems mentioned above is illustrated in Fig. 12. Note that $In_xGa_{1-x}As$ alloys can be lattice-matched with an appropriate $In_yGa_{1-y}P$ alloy to provide emission at any desired wavelength between 0.9 and 1.7 μm. In general, lattice matching occurs for $In_xGa_{1-x}As$ and $In_yGa_{1-y}P$ when $y \sim 0.97 x + 0.49$.

The energy-bandgap values for alloys of $In_yGa_{1-y}P$ and $In_xGa_{1-x}As$ at their lattice-matching compositions are shown in Fig. 13. The energy-bandgap difference of 0.4-0.5 eV shown here is sufficient to provide strong electron confinement in the low-energy material (InGaAs). A similar difference in refractive index for these materials (not illustrated) serves to confine light in InGaAs that is prepared in a waveguide structure between confining layers of InGaP. The energy-bandgap and refractive-index steps discussed above form the basis of fabricating heterojunction emitters (both edge-emitting LEDs and lasers). Efficient room-temperature heterojunction lasers of InGaAs/InGaP with threshold
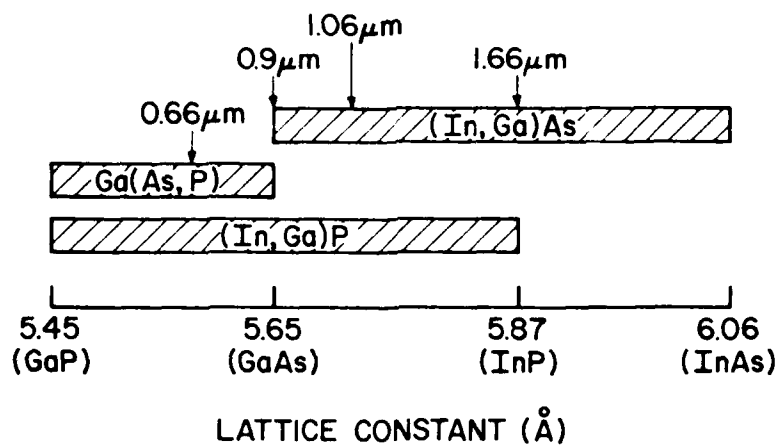
Figure 12. Lattice parameters of InGaAs and InGaP alloys.
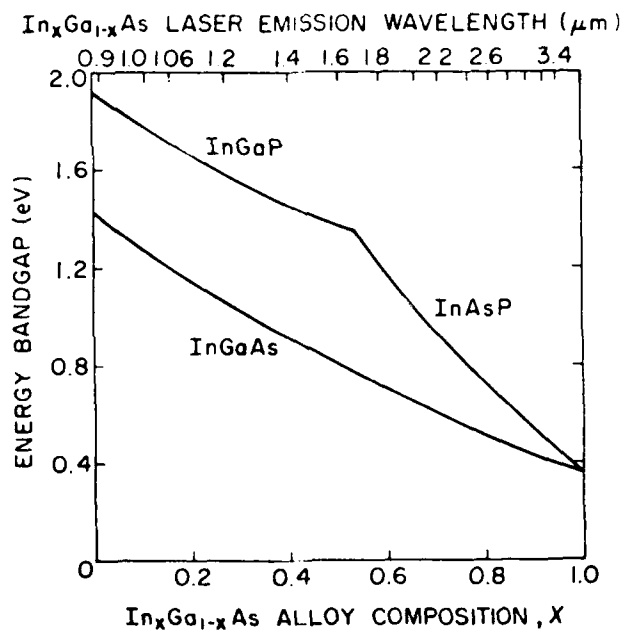
Figure 13. Energy bandgap of InGaAs and InGaP alloys.

current densities as low as 1000 A/cm^2 and differential quantum efficiencies as high as 55% have, in fact, been prepared [8].

8. C. J. Nuese, G. H. Olsen, M. Ettenberg, J. J. Gannon, and T. J. Zamerowski, Appl. Phys. Lett. 29, 807 (1976).

B. QUATERNARY InGaAsP/InP STRUCTURES

The ternary heterojunction structures described in the previous section have yielded excellent devices but suffer from three limitations:

(1) They require close compositional control of <u>three</u> successive ternary epitaxial layers.

(2) They require a compositional grading layer between the substrate and the epilayers.

(3) Thermal expansion coefficient differences lead to a built-in strain between the growth temperature and room temperature <u>even for supposedly lattice-matched structures</u>.

Most of these shortcomings can be circumvented by the use of appropriate quaternary alloys. Such materials have one degree of freedom more than ternary alloys, thereby allowing the <u>independent control of energy bandgap and lattice constant</u> over rather wide ranges.

In the three-dimensional drawing of Fig. 14, we illustrate the dependence of the energy bandgap on alloy composition for the quaternary alloy InGaAsP. This system is bounded on four sides by the ternary alloys InGaAP, InGaAs, GaAsP, and InAsP. The solid curves running approximately horizontally across the alloy system are constant-bandgap curves, and are seen to vary between 0.36 and 2.2 eV over the direct-bandgap portion of this alloy. The small GaP-rich portion of the alloy at the top of the illustration has an indirect energy-band structure. In principle, the InGaAsP system can provide wavelengths between 0.55 and 3.4 μm at room temperature.

Of particular importance to our discussion are the iso-lattice-constant curves, which are dashed in Fig. 14. Any single iso-lattice-constant curve is seen to cross several iso-bandgap curves, illustrating that quaternary alloys with appreciably different energy-bandgap values (or refractive-index values) can be obtained without altering the lattice constant of these materials. For example, the 5.869-$\mathring{A}$ iso-lattice-constant line originating at InP intersects energy-bandgap curves between 1.35 and 0.74 eV, which correspond to operating wavelengths between 0.92 and 1.67 μm.

Based on the discussion above, a simple quaternary heterojunction LED or laser structure can be used for the same wavelength range (0.92 to 1.7 μm) as the InGaAs/InGaP ternary structure discussed previously. Here, the substrate would be InP, as also would be the confining layers. By altering the alloy

17
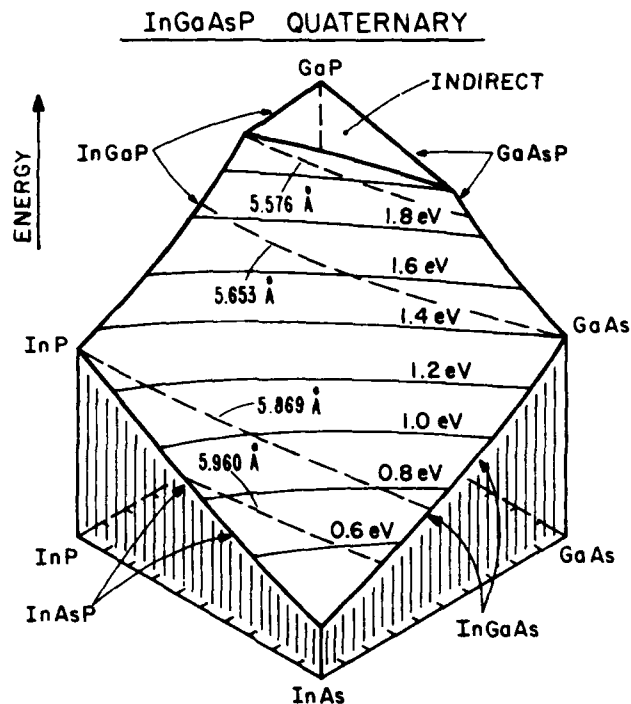
Figure 14. Energy bandgap and lattice parameter vs composition
            InGaAsP alloys.

composition of the InGaAsP active layer, the operating wavelength can be var-
ied while maintaining close lattice matching across the entirety of the struc-
ture. Note that the quaternary structure requires close compositional control
of only a single InGaAsP layer, and does not require a compositional grade,
since it exactly matches the lattice constant of InP. The single limitation of
the InGaAsP/InP structures is the inferior quality of InP substrates (relative
to GaAs). However, this situation will undoubtedly improve with time, and low-
dislocation-density material is already available from select laboratories (if
not commercially).

V. EDGE-EMITTING LEDs

A. TERNARY InGaAs/InGaP EDGE-EMITTING LEDs

Vapor-grown InGaAs/InGaP heterostructures that emit light near 1.06 µm
have been fabricated into edge-emitting LED structures of the type shown in
Fig. 15(a). These materials were of reasonable quality, since lasers also
were prepared from them with very low threshold current densities (1000 to
1500 A/cm^2 with cw room-temperature operation observed) however, their active
regions were 0.1 to 0.2 µm thick. A summary of the LED parameters obtained
from several ternary structures is presented in the top portion of Table 1.
One observation is that the power emitter per unit <u>contact</u> area is much greater
for the stripe-contact (10 µm wide) geometry than for the broad-area contact
(100 µm wide). It should be noted that over 1 mW of power has been obtained
from one ternary structure at a dc current of 200 mA with a power efficiency
of almost 0.5%, as illustrated in Fig. 16.

B. QUATERNARY InGaAsP/InP EDGE-EMITTING LEDs

1. VPE Structures

The vapor-phase growth technology of InGaAsP alloys has been optimized
under a separate government contract (DAAB07-76-C-0872-DARPA) at RCA Laborator-
ies. The results of this study have been applied to the growth of InGaAsP/InP
heterojunction LEDs. The actual structure is shown in Fig. 15(b). A summary
of the LED power output and efficiency values for these devices also is pre-
sented in Table 1 for wavelengths of 1.12 and 1.29 µm. Again, the superior
power "density" (per unit contact area) is demonstrated with the stripe-contact
geometry as opposed to the broad-area contact. A power output of 1.2 mW with
an efficiency of ∿0.6% has been attained in a quaternary LED structure which
emits light at 1.27 µm. The dc power-current characteristic of this LED is
shown in Fig. 16 and it compares well with that of our earlier ternary hetero-
junction devices. The deviation from linearity at high currents is due to de-
vice heating. The quaternary structure from which such LEDs were prepared also
yielded laser with broad-area threshold currents below 2000 A/cm^2 at room tem-
perature. Room-temperature cw operation with threshold currents as low as
85 mA have been obtained from such structures with 12-µm oxide-stripe defined
contacts [9].

---

9. G. H. Olsen, C. J. Nuese, and M. Ettenberg, Appl. Phys. Lett. <u>34</u>, 262 (1979).
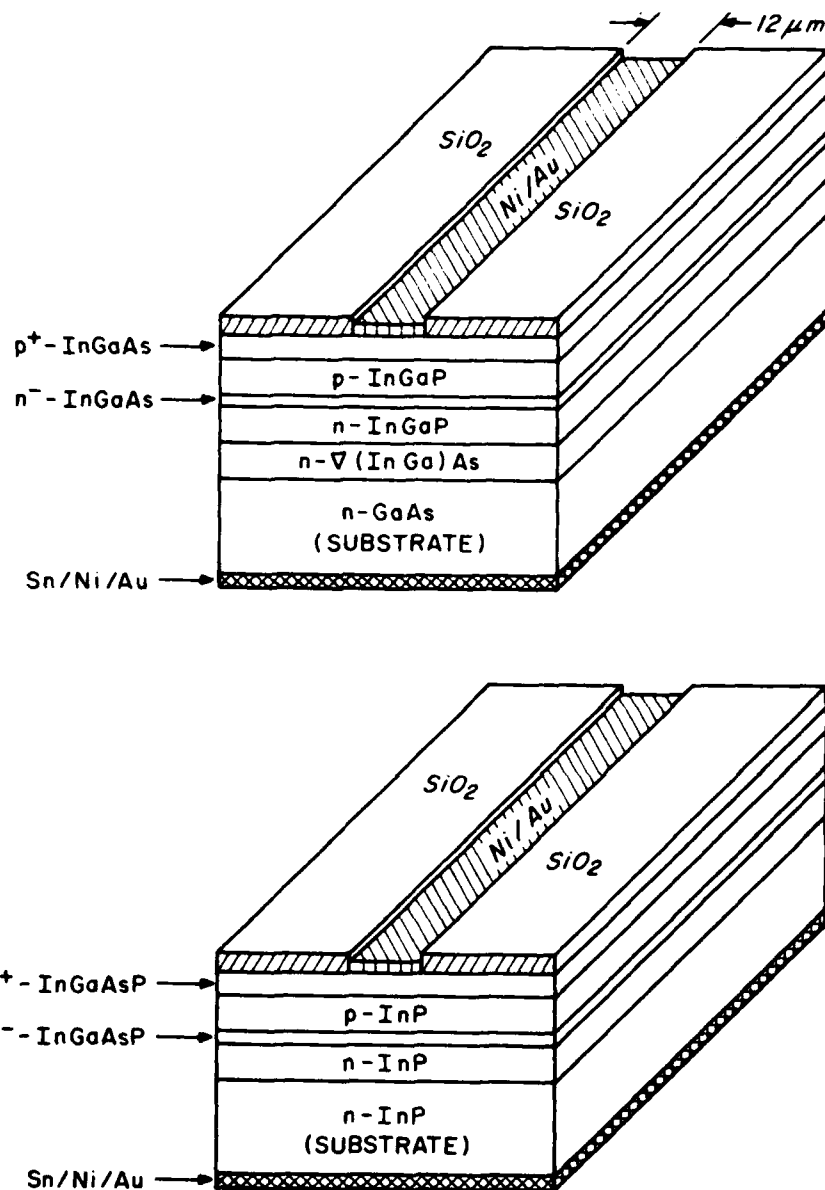
Figure 15. Sketch of device structures used for ternary and quaternary LEDs.

We have also prepared a series of vapor-grown InGaAsP/InP double-hetero-junction LEDs having emission wavelengths in the range of 1.1 to 1.4 μm. A summary of typical LED output power vs input dc current is shown in Fig. 17 for three edge-emitting devices that emit light at 1.1, 1.25, and 1.4 μm. The structures have either broad-area contacts (in which the entire 100- by

TABLE 1. OUTPUT POWER AND EFFICIENCY FOR TERNARY AND QUATERNARY VPE LEDs.

Sample No.	Power per Contact Area (W/cm^2)	Geometry*	Power @ 100 mA (mW)	Power @ 200 mA (mW)	Contact Area (μm × μm)	Efficiency (%)	λ (μm)
Ternary InGaAs/InGaP							
1388B	0.50	B-A	0.160		100 x 300	0.14	1.057
	1.81	S	0.056		10 x 310	0.09	1.057
1647	0.98	B-A	0.305	0.610	110 x 280	0.27	1.049
	15.40	S	0.231		10 x 150	0.19	1.049
1649	0.57	B-A	0.172		100 x 300	0.14	1.036
	15.30	S	0.540	1.07	10 x 175	0.45	1.036
Quaternary InGaAsP/InP							
1946	1.10	B-A	0.385	0.740	100 x 350	0.48	1.12
	17.00	S	0.342		10 x 200	0.47	1.12
5050	0.57	B-A	0.170		100 x 300	0.14	1.29
	2.00	S	0.060		10 x 300	0.06	1.29
5052	1.97	B-A	0.590	1.20	100 x 300	0.61	1.29

*B-A = Broad Area
S = Stripe
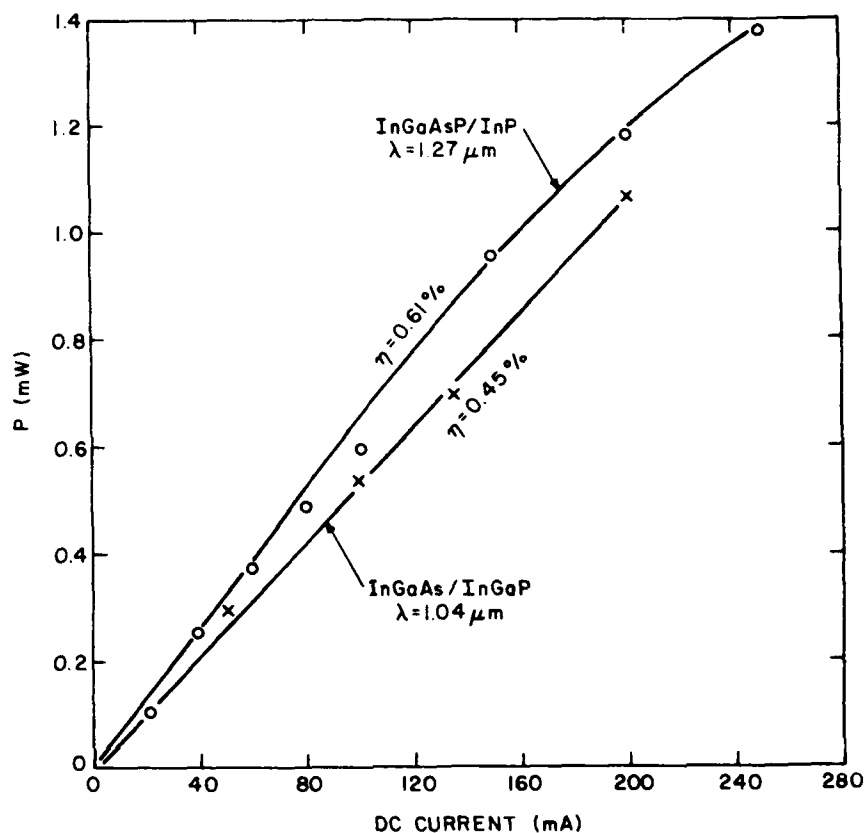
Figure 16. Power emission vs dc current from InGaAs/InGaP and InGaAsP/InP VPE edge-emitting LEDs.

300-µm top area of the diode is contacted with metal) or 12-µm oxide-stripe-defined contacts. The spectral emission for a 1.28-µm LED is shown in Fig. 18. The peak wavelength is 1.29 µm and the halfwidth is 600 Å. This wavelength is close to that needed for operating at the minimum value of dispersion in typical silica fibers. However, this halfwidth was narrower than most; typically 700 to 750 Å was observed. This point is discussed further in Section VII.

2. LPE Structures

High-quality LED structures also were prepared via liquid-phase epitaxy as described in Section III. Efficiencies above 0.3% were routinely observed, and values as high as 0.7% at 100 mA were obtained. Figure 19 contains a plot of output power vs drive current from one of our best structures. Other results are presented in Section VII. The spectral characteristics from LPE edge emitters are discussed further in Section VIII.

22
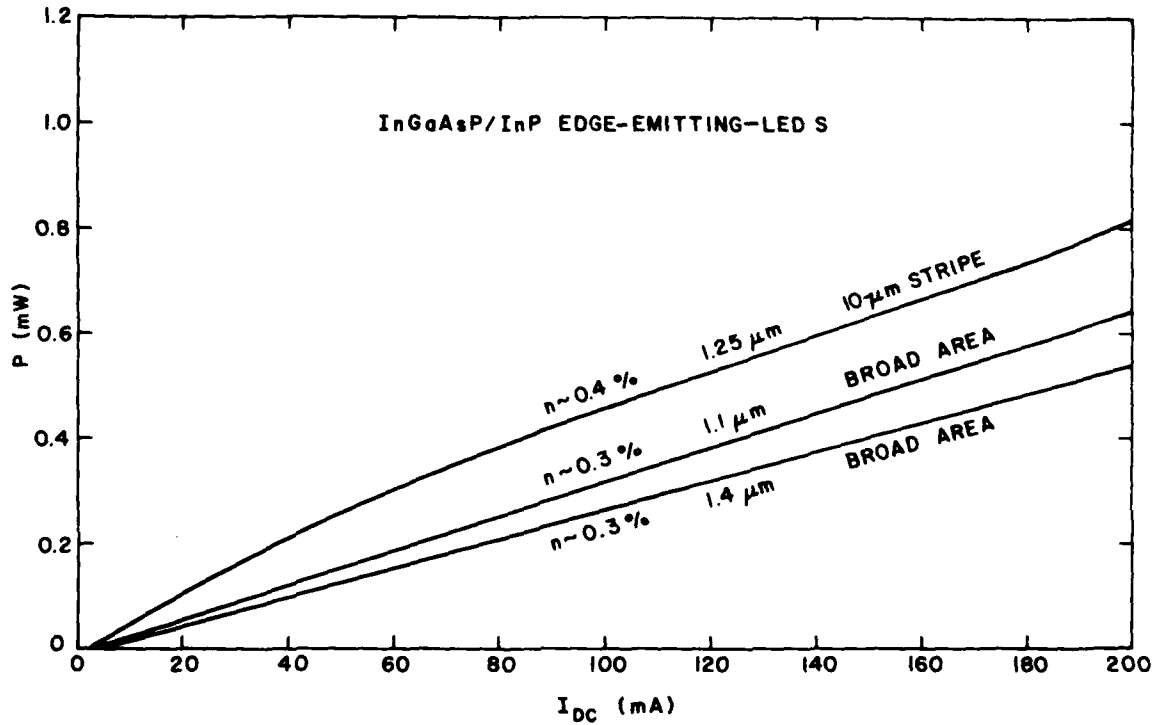
Figure 17.   Output power vs input dc current for ı.12-, 1.25- and 1.40-μm edge-emitting LEDs.
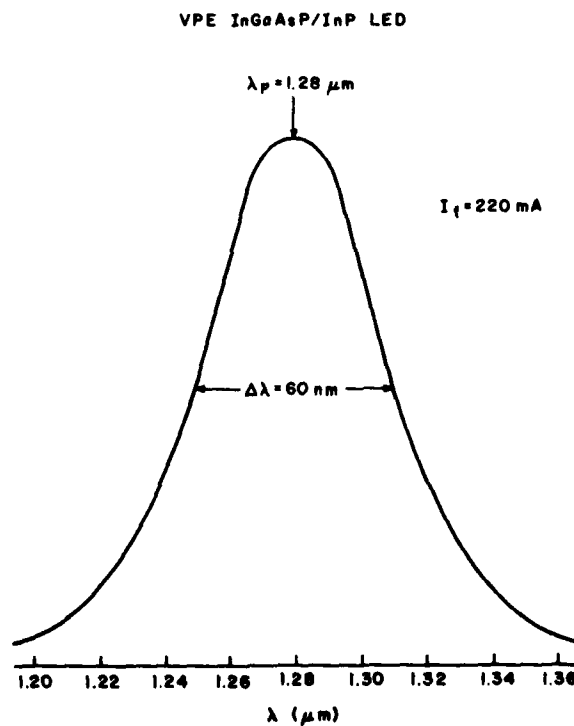
Figure 18.   Spectral emission curve for 1.28-μm InGaAsP/InP VPE LED.

23
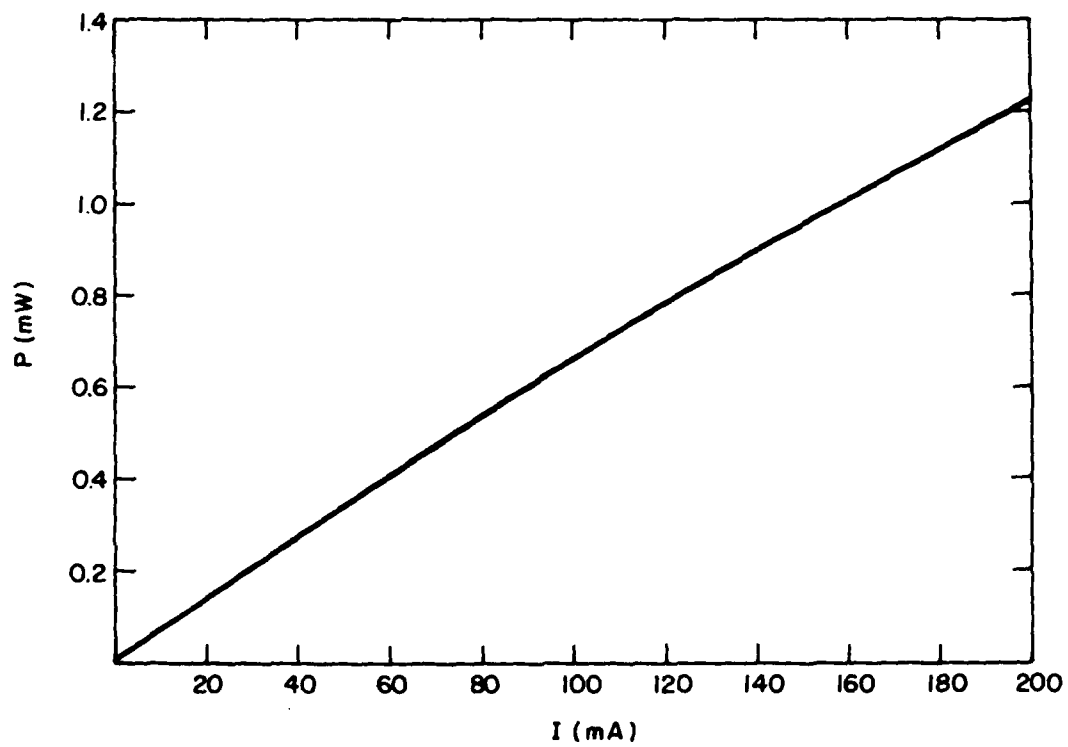
Figure 19.   Output power vs input dc current of an LPE LED.

VI.   SURFACE-EMITTING LEDs

Both Marcuse [10] and Botez and Ettenberg [11] have concluded that under most conditions, notably for high data rates and low NA fibers, more power can be coupled into an optical fiber from an edge-emitting LED rather than surface-emitting LEDs. Nevertheless, surface emitters were prepared under this contract in order to carry out a comparison of the two structures made from InGaAsP/InP alloys which emit light near 1.3 μm.

Another drawback of the surface emitter is the complexity of its fabrication. Compare the process steps of the two structures:

Edge-Emitter Fabrication

1.   Deposit SiO_2 on p-side.
2.   Apply photoresist (PR) to p-side.
3.   Expose 12- or 65-μm stripes through PR.
4.   Etch stripes in SiO_2 with buffered HF.
5.   Remove PR.
6.   Evaporate Sn on n-side.
7.   Electroplate Ni/Au in stripes on p-side and on n-side.
8.   Evaporate Cr/Pt/Au over entire p-side.
9.   Lap n-side to 100-μm thickness.
10.   Cleave chips and mount.

Surface-Emitter Fabrication

1.   Evaporate Au/Zn on p-side.
2.   Apply photoresist (PR) and define 50-μm dots.
3.   Etch off Au/Zn leaving 50-μm contact dots.
4.   Remove PR.
5.   Apply SiO_2 over entire p-side at 350°C (this also sinters in Au/Zn).
6.   Lap substrate to 100-μm thickness.
7.   Apply SiO_2 to n-side.
8.   Apply PR to n-side.
9.   Align 200-μm hole mask on n-side with 50-μm dots on p-side.
10.   Remove SiO_2 on n-side leaving 200-μm SiO_2 dots.

10.   D. Marcuse, IEEE J. Quantum Electron. QE-13, 819 (1977).
11.   D. Botez and M. Ettenberg, (J. Quantum Electron. QE-15, 1230 (1979)).

11. Remove PR.

12. Evaporate Sn on n-side (does not stick to SiO_2).

13. Remove SiO_2 on n-side with buffered HF.

14. Apply PR to p-side.

15. Align mask with 50-µm p-contact dots and etch holes to expose dots.

16. Remove SiO_2 from p-contact dots.

17. Remove PR.

18. Plate Ni/Au on p- and n-side.

19. Apply Cr/Pt/Au to entire p-surface.

A sketch of the surface-emitting structure is shown in Fig. 20. Note that in addition to having more process steps (17 vs 10), the surface emitter requires three photoresist steps vs one for the edge, and that two of the three steps require precise alignment.
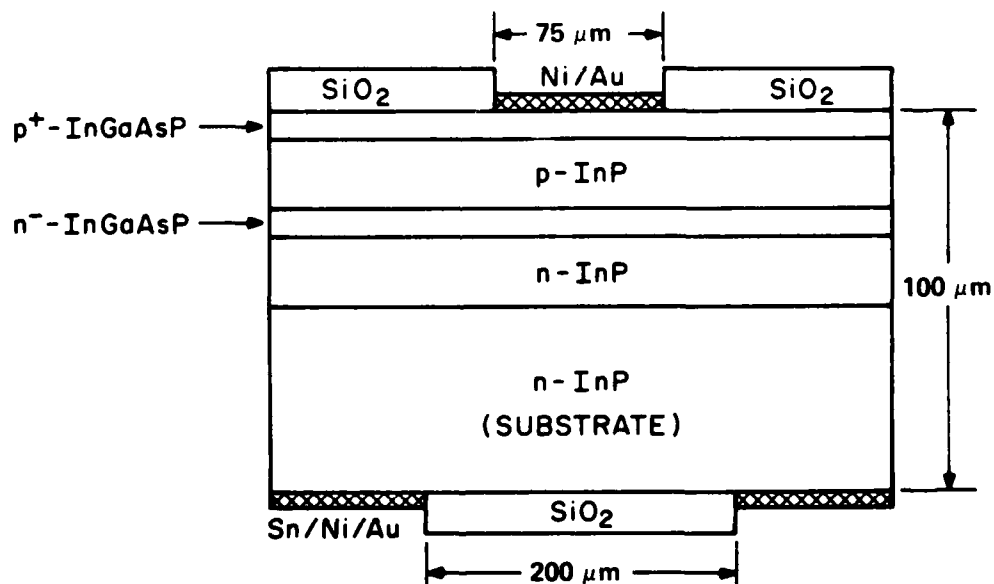
Figure 20. Schematic representation of a surface-emitting LED structure.

Surface-emitting LEDs were fabricated from both LPE and VPE wafers. The best results obtained with each structure are shown in Fig. 21. More power was obtained from the LPE structure as compared to the VPE structures (i.e., initial power efficiencies of 1.6% vs 1%). The deviation from linearity at high currents is due to device heating.
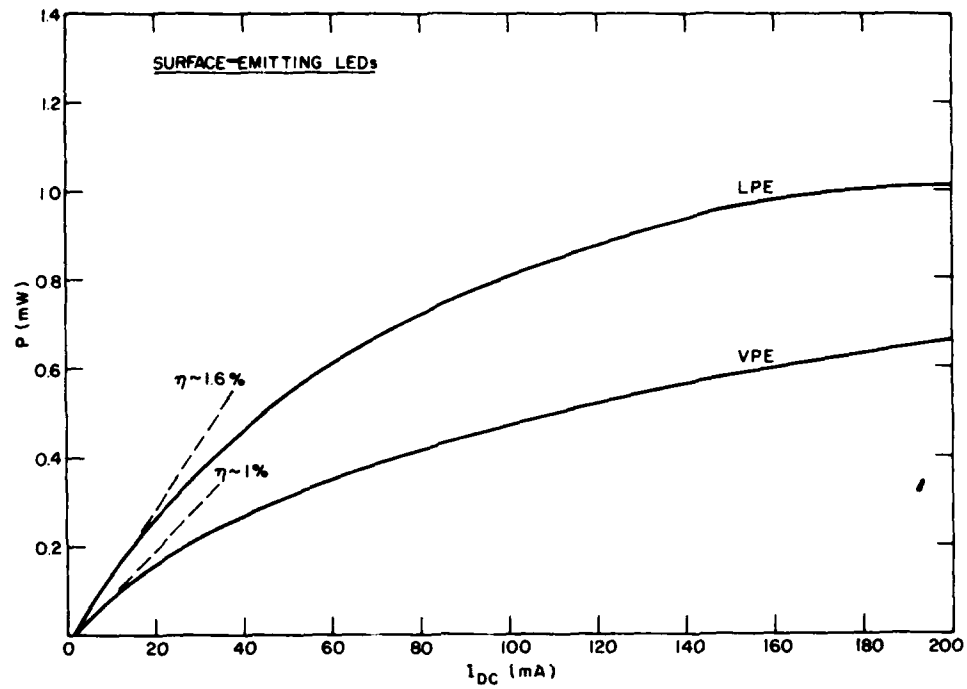
Figure 21. Output power vs input current for LPE and VPE surface-
emitting LEDs.

Although we do not feel that our surface emitter is optimized yet, it
clearly is more efficient than the edge-emitting structure.

VII. COMPARISON OF SURFACE- AND EDGE-EMITTER SPECTRAL DISTRIBUTIONS

Figures 22 and 23 show comparisons of the spontaneous emission spectra of both VPE and LPE surface- and edge-emitting LEDs. These experiments were particularly difficult to perform in that material had to be cut from the same wafer to make the comparison meaningful, and most of the material is consumed in the fabrication of surface emitters. Both VPE and LPE edge emitters had spectral halfwidths on the order of 64 meV, while the surface emitters had halfwidths on the order of 110 meV. This difference in halfwidths was discussed in detail by Dyment et al. [12]. By measuring the light emission from both the top surface and the perpendicular facets of a specially constructed surface-emitting LED, they determined that three separate peaks could be observed: one from the surface (λ_1), and two from the edge emission (λ_2 and λ_3) (see Fig. 22). The shortest wavelength peak was λ_1 since it underwent the least amount of absorption. The two edge-emission peaks come from light that passed (i) through the transparent combining layer (λ_2), and (ii) through the absorbing cavity layer (λ_3). Thus, λ_2 is only slightly longer than λ_1, whereas λ_3 is usually shifted two or three hundred angstroms to longer wavelengths due to the preferential absorption of the shorter wavelengths. The two peaks λ_2 and λ_3 often overlap - especially for heavily doped layers - and sometimes appear as one broad peak rather than two separable peaks. The fact that this peak shift was not observed between our LPE surface and edge emitters is not understood. Poor heat-sinking may have caused the surface-emission peak to shift to longer wavelengths and thus coincide with edge-emitter peaks. Dyment points out that since the emission from the edge emitter has to travel through hundreds of microns of the absorbing cavity, its spectral halfwidth will be reduced substantially compared to that of the surface emitter which undergoes no similar absorption. Since the shorter wavelengths get absorbed more readily than the longer ones, the peak wavelength of the edge emitter might be expected to occur at longer wavelengths than the surface emitter as shown in Fig. 22 for the VPE emitters. Our conclusion is that independent of the source of the material, edge-emitting LEDs will exhibit substantially narrower spectral widths than surface emitters. This becomes particularly important for LED use in fiber optical communications where the spectral dispersion of fiber is usually the limiting parameter.

12. J. C. Dyment, F. P. Hapron, and A. J. Springthorpe, IEEE Trans. Electron Devices ED-24, 995 (1977).

VPE EDGE AND SURFACE-EMITTING LEDs
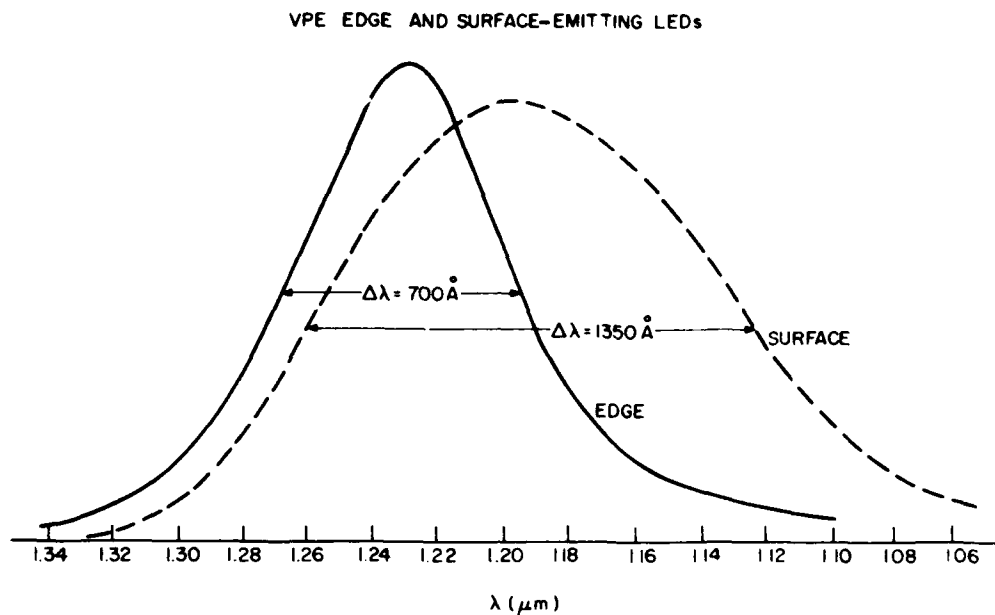
Figure 22. Spectral emission characteristics of an edge- and surface-
emitting LED prepared from a VPE wafer.

SPECTRA FROM LPE GROWN SURFACE
AND EDGE-EMITTING LEDs
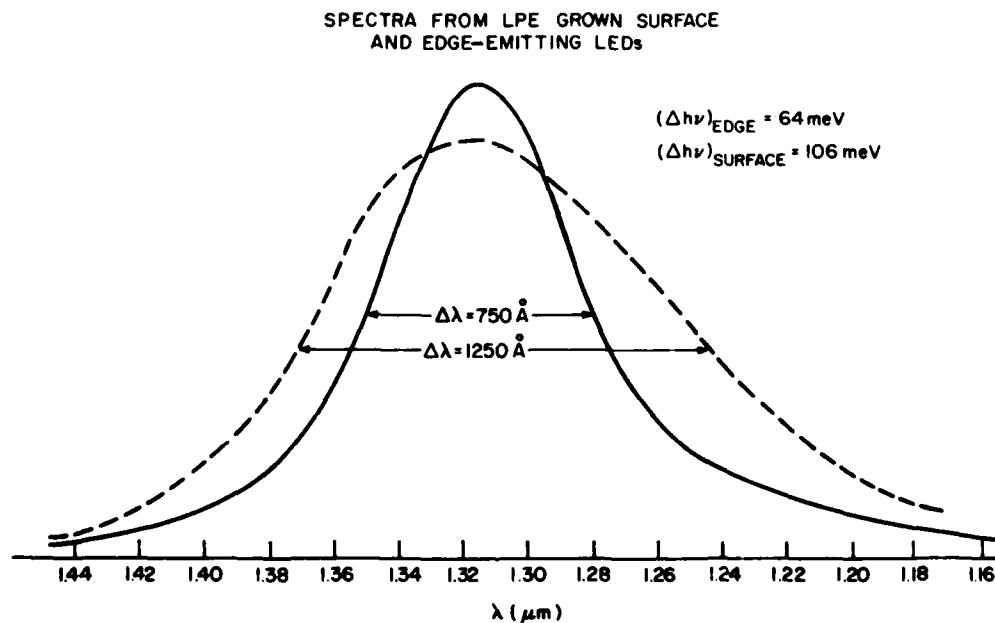
Figure 23. Spectral emission characteristics of an edge- and surface-
emitting LED prepared from a LPE wafer.

29

VIII.   COUPLING OF 1.28-μm LED EMISSION INTO AN OPTICAL FIBER

Coupling experiments have been performed to determine the maximum amount of optical power that can be coupled from a 1.28-μm VPE edge-emitting LED into a 0.2-NA graded-index fiber with a 50-μm core diameter. The fiber was treated with a mode-stripping agent to prevent the light trapped in the cladding from being measured. The fiber end was balled and placed in close proximity to the LED edge. Figure 24 contains a plot of coupled power into the fiber versus LED drive current. Note that over 80 μW was coupled into the fiber at a drive current of 200 mA. This value already represents a significant advance over the present long-wavelength LED technology, since presently available LEDs (of InGaAs) usually are limited to less than 10 μW coupled into a typical fiber.
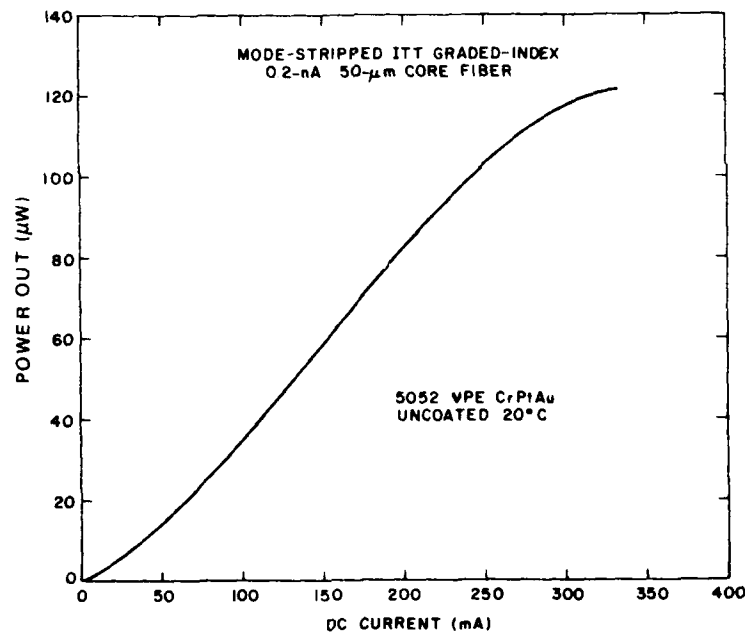
Figure 24.   Optical power coupled into a mode-stripped 50-μm core diameter
0.2-NA optical fiber vs dc input current supplied to a 1.25-μm
edge-emitting LED.

IX. RISE TIME AND BANDWIDTH MEASUREMENTS

A. PULSE MEASUREMENTS

The rise and fall times for the optical output were determined from meas-
urements of the optical pulse response of the LEDs. The LED under test was con-
nected in series with a 50-Ω resistor and a capacitor to provide a 50-Ω ac im-
pedance and dc bias isolation from the pulser. The optical output was detected
with a germanium avalanche photodetector and recorded on a sampling oscilloscope.
Figure 25 shows a typical recording of current pulse and optical response.
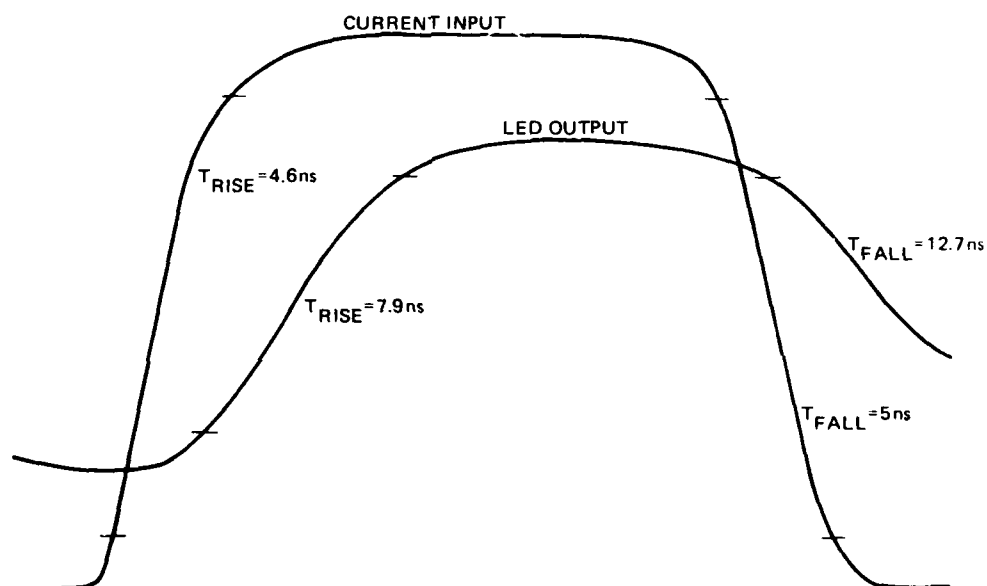
Figure 25.   Typical rise and fall times for the input current pulse and
output light pulse applied to a VPE edge-emitting LED.

Pulse rise and fall times were defined as the time interval between 10%
and 90% of full output. Correction for the rise and fall time of the current
pulse was made according to the formula

$$T_{response} = \sqrt{T_{measure}^2 - T_{pulse}^2}$$

when $T_{response}$ is the rise or fall time of the LED, $T_{measure}$ that of the measure-
ment, and T_{pulse} that of the current pulse. The results of measurements on a
review of LEDs are given in Table 2. One should note that the rise times of LEDs
are generally functions of pulse current, while fall times are independent of
pulse current. Fall times were in the range 9-12 ns.

TABLE 2. LED RISE- AND FALL-TIME DATA

Type	LED	i_{bias} (mA)	i_{pulse} (mA)	T_{rise} (ns)	T_{fall} (ns)
LPE Edge	954 II13	8.9	60	9.3	11.8
LPE Edge	954 I12	8.4	60	10.0	9.4
LPE Surface	932 II3	5.5	60	6.4	11.7
LPE Surface	932 II1	8.3	60	10.7	11.8

B. FREQUENCY RESPONSE MEASUREMENTS

The optical response as a function of frequency was also measured using the same isolation and impedence matching circuit as for the pulse measurements. A typical response curve is shown in Fig. 26. The solid line represents the function

$$R = \frac{1}{\sqrt{1 + \left(\frac{f}{f_o}\right)^2}}$$

which represents the frequency dependence of LED response. Table 3 gives the results of various measurements. The frequency at which the LED modulated optical output dropped to one-half the low frequency value was in the range 65 to 100 MHz.
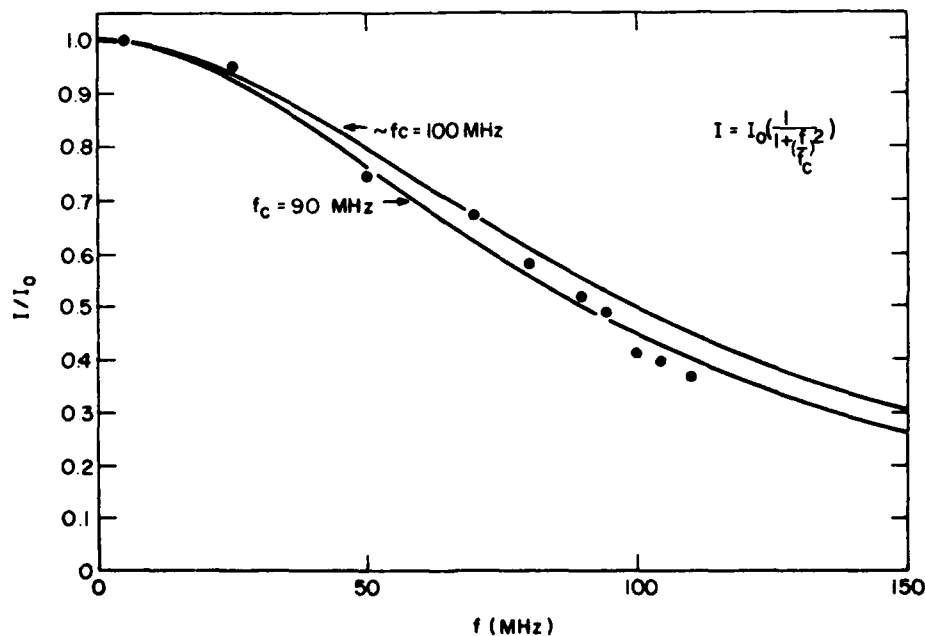
Figure 26. Typical frequency response of a VPE edge-emitting LED.

32

TABLE 3. LED FREQUENCY RESPONSE DATA

Sample #	i_{bias} (mA)	i_{pp} (mA)	$f_{1/2}$ (MHz)
5103 J1	100	60	84
5052 I16	100	60	65
5131 C4	150	60	85
5131 C-8	150	60	90
5131 C-5	150	60	100

As high as 200 mA. No change in fall time with increased current.

Some typical fall times for VPE LEDs were:

Type	#	T_{fall}(ns)
VPE edge	5103	8
VPE surface	5157	10

X. COMPARISON OF AlGaAs SURFACE- AND EDGE-EMITTING LEDs

As we have already indicated, there are two practical geometries for fiber-compatible heterojunction LEDs, surface emitters and edge emitters. Both geometries are being developed under this program, with the edge emitters already having provided encouraging results (as described in the preceding section). However, to separate the effects of geometry from fabrication technique, a comparison can be made of surface- and edge-emitting LEDs of AlGaAs, where the material and fabrication techniques are fully developed. Such a study was briefly undertaken during the past quarter, with the reports described in more detail below. A publication based on these results has been prepared [11] and is included in the Appendix.

Highest power levels (into air) have been reported [13] for a Burrus-type surface emitter. However, due to its wide (Lambertian) beam pattern, the coupling efficiency of a surface emitter to a fiber is poor. Surface-emitting LEDs are advantageous primarily for fibers with large acceptance angles (large values of numerical aperture) and large core diameter. As shown in Fig. 27 which includes calculated coupling efficiencies as well as our own coupling data for RCA's surface and edge emitters of AlGaAs, the coupling losses are about 17 dB for a surface emitter into a 0.2-NA fiber. On the other hand, an edge-emitting LED has a very high radiance due to the combination of a very small emission area (typically 10 μm x 0.1 μm) and a narrow beam pattern. Such a geometry is especially advantageous for fibers with small acceptance angles, and coupling losses into a 0.2-NA fiber are only about 10 dB. From the known beam patterns of the two types of devices and the best absolute emission power levels reported in the literature for AlGaAs heterojunction LEDs, the maximum power coupled into a fiber can be calculated versus the numerical aperture of the fiber, as shown in Fig. 28. Here, we see that an edge emitter is advantageous for fibers with numerical aperture values less than 0.4. This conclusion is consistent with RCA's independent observation with AlGaAs surface emitters and edge emitters, where we find we can couple higher power levels into low-NA fibers with an edge emitter.

13. C. A. Burrus and B. I. Miller, Opt. Commun. 4, 307 (1971).
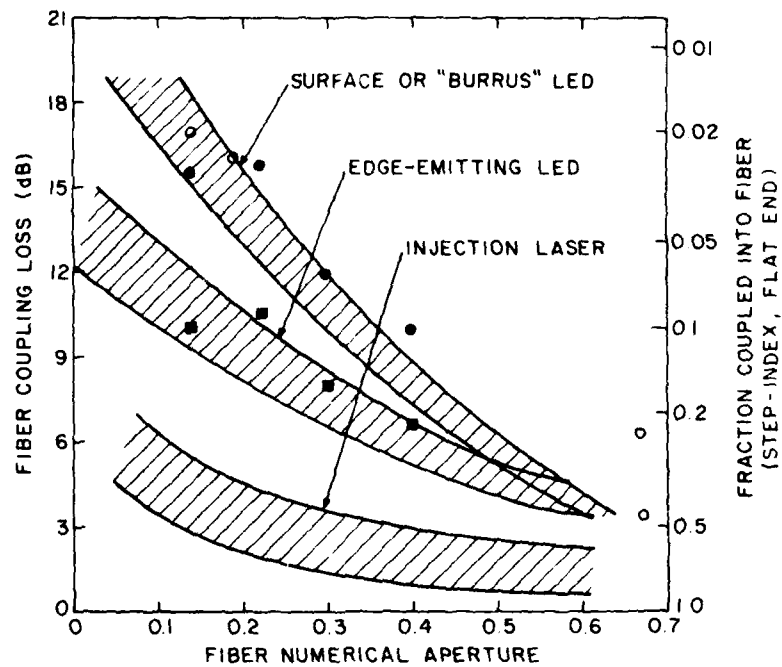
Figure 27. Calculated coupling efficiency of edge-and surface-emitting
LEDs as a function of numerical aperture.
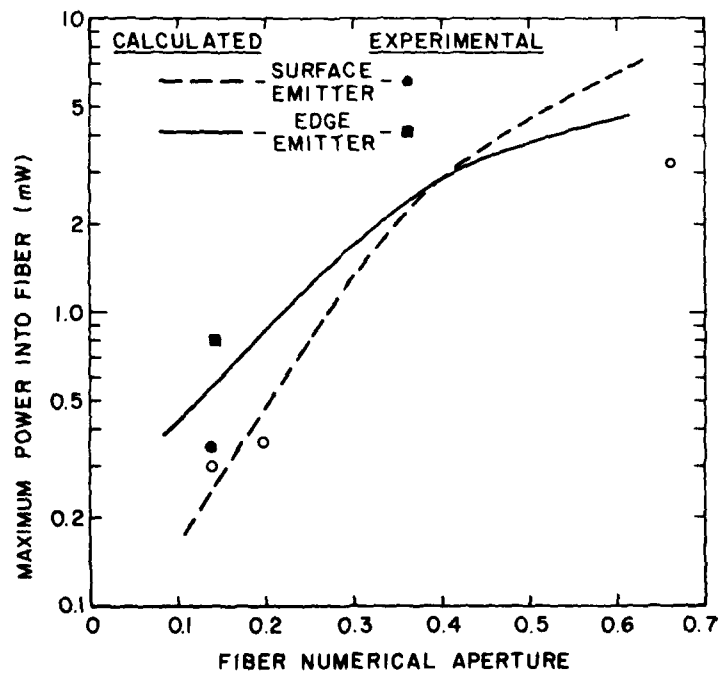
Figure 28. Maximum power coupled into a fiber vs numerical aperture
for edge-and surface-emitting LEDs.

Another important difference between surface and edge emitters is their modulation capabilities. Shown in Fig. 29 is the pulse response of surface- and edge-emitting LEDs of AlGaAs to current pulses at data rates between 10 and 50 Mbit/s. Whereas the response time of surface LEDs appears to be limited to less than 20 to 25 Mbit/s, the edge-emitting LEDs readily follow the current pulses at the 50-Mbit/s rate illustrated in Fig. 29. Other data, in fact, indicate that the AlGaAs edge-emitting LEDs can follow data pulses at least up to 150 Mbit/s.

The results described here are for state-of-the art AlGaAs devices emitting at 0.82 μm; however, the conclusions hold with respect to all double-heterojunction structures, and are just as valid for the InP/InGaAsP structures of primary interest in this program.
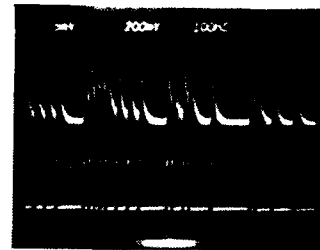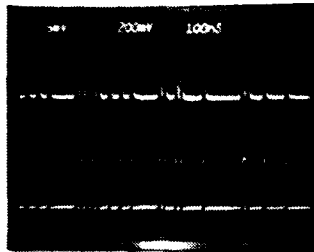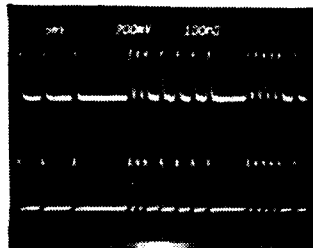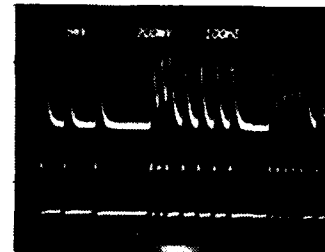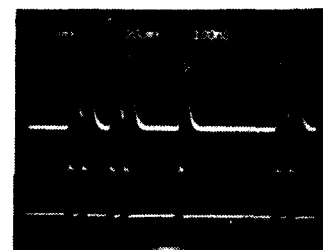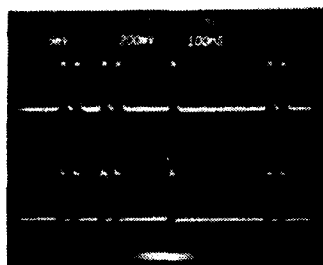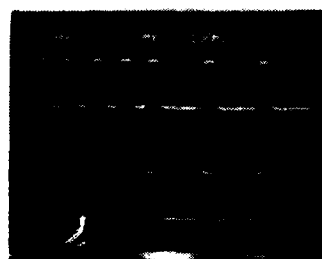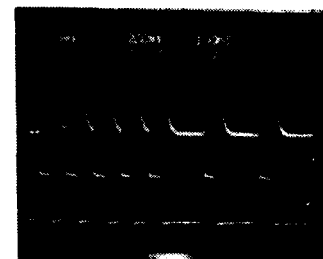
Figure 29. Modulation capability of edge- vs surface-emitting AlGaAs LEDs.

A. REPRODUCIBILITY

Under a separate DARPA Contract No. DAAB07-76-C-0872 our VPE system has been completely automated in an attempt to improve the reproducibility of vapor-grown devices.

A complete double-heterojunction laser structure can now be grown by pre-programming all steps on a microprocessor; no operator attention is required during the two-hour run time. The unit is controlled by a Tylon Process Controller, which can store 16 independent SPDT relay positions for up to 99 different timing steps.

All gas-control valves are actuated by air-operated solenoid valves, which, in turn, are actuated by remote electrical solenoids (to eliminate the danger of sparking near flammable gases). All reactant gases are controlled by electrically operated mass-flow controllers. Insertion and removal of a zinc bucket (for p-type doping) is accomplished via a magnetic feedthrough which is raised or lowered by an electric motor. Substrate position is controlled by a motorized belt drive, which has three stop positions (forechamber, preheat, and growth). A photograph of the system is shown in Fig. 30. Control of each layer of a heterojunction device structure is accomplished via five potentiometers (for the HCl-In, HCl-Ga, PH_3, AsH_3 and H_2S mass-flow controller settings).

Figure 30. Photograph of the automated VPE reactor.

Up to five separate layer settings can be programmed. Even more layers can be grown if only doping changes are required.

In order to carry out a run, all steps (relay positions and times) are first programmed into the process controller. Once stored, this data can be kept indefinitely or changed at will. Thereafter, once a fresh substrate is loaded into the forechamber, an operator merely activates the "start" button, and returns two hours later to receive the fully grown heterostructure. Several runs have already been made with the new automated system, and flawless mechanical performance has been observed in all cases. The structures have been found to provide fairly good device performance, and are presently being optimized. Our hope is that devices prepared in this fashion (once optimized) will have a reproducibility that was previously unattainable.

It is too early to tell whether or not a significant increase in device reproducibility has resulted from the automation of our reactor. At present, approximately 50% of all vapor-grown devices have LED efficiencies of 0.3% or more. Interestingly, the reproducibility of LED efficiency for device prepared by liquid-phase epitaxy appears to be even better than that for the vapor-phase epitaxy. Table 4 contains a summary of recent LPE device results. Out of 31 wafers, over 19 had power efficiencies greater than 0.3%. These results were obtained using a "clip"-type contact. Values would undoubtedly be higher if proper heat sinking was used.

A typical example of the reproducibility of devices made from the same VPE wafer is shown in Table 5 (for 22 LEDs made from the same wafer). All devices underwent the same processing and mounting procedures. The output power (mW) of these devices at 100-mA drive current (which here is fortuitously equal to the external power efficiency in percent) is consistently over 0.3 mW, and all fall within the range 0.3 to 0.5 mW. The output power measured at 200 mA is less than twice that at 100 mA due to poor heat sinking; double the value could be obtained when improved heat sinking was used.

Other output data from additional devices made from this wafer are also included in Table 6.

B. RELIABILITY

Under a separate contract (ERADCOM Ft. Monmouth #DAAB07-77-C-2173) a reliability study was undertaken on our 1.06- and 1.3-μm lasers and LEDs. This study showed that the LED reliability of VPE quaternary alloy devices which

TABLE 4. LED EFFICIENCY FOR A SERIES OF LPE InGaAsP/InP
DOUBLE-HETEROSTRUCTURE WAFERS

Sample No.	η_{LED}(%)
909	0.35
910	0.17
917	0.33
918	0.33
919	0.50
920	0.07
921	0.03
922	0.27
923	0.33
924	0.30
925	0.03
927	0.15
928	0.22
929	0.30
930	-
931	0.40
932	0.60
933	-
934	-
936	0.50
937	0.35
938	0.35
939	0.60
941	0.33
942	0.43
944	0.35
948	0.40
950	0.05
951	0.15
953	
954	

(cw 1st LPE laser)

emit at these wavelengths looked exceptionally promising. Figures 31 and 32
contain plots of light output vs operating lifetime for several 1.1-μm laser
structures emitting in the spontaneous mode at room temperature for over
10,000 h, and for 1.25-μm lasers emitting spontaneously at 70°C for almost
9000 h. No significant degradation has been observed in either case [14].

---

14. H. Kressel, M. Ettenberg, and I. Ladany, Appl. Phys. Lett. 32, 305 (1978).

40

TABLE 5.   OUTPUT POWER AS A FUNCTION OF INPUT dc CURRENT FOR 22 VPE
1.24-μm LEDs CUT FROM THE SAME WAFER

Diode #	Mount	Stripe	$I_p = 100$ mA P mW (=%η)*	$I_f = 200$ mA dc P mW
L1	OP-4	9xST	0.309	0.400
L2	OP-4	9xST	0.497	0.708
L3	OP-4	9xST	0.355	0.502
L4	OP-4	9xST	0.443	0.609
L5	OP-4	9xST	0.442	0.608
L6	OP-4	9xST	0.364	0.502
L7	OP-4	9xST	0.384	0.513
L8	OP-4	9xST	0.463	0.642
L9	OP-4	9xST	0.446	0.611
L10	OP-4	9xST	0.474	0.655
L11	OP-4	9xST	0.470	0.643
L12	OP-4	9xST		
L13	OP-4	12xST	0.395	0.579
L14	OP-4	12xST	0.356	0.514
L15	OP-4	12xST	0.368	0.541
L16	OP-4	12xST	0.345	0.513
L17	OP-4	12xST	0.324	0.457
L18	OP-4	12xST	0.453	0.690
L19	OP-4	12xST	0.320	0.437
L20	OP-4	12xST	0.343	0.458
L21	OP-4	12xST	0.375	0.527
L22	OP-4	12xST	0.368	0.505

*For 1.25-μm emission with 100-mA drive current, $P(mW) \simeq \eta(\%)$.

Similar accelerated lifetest results have been reported in the literature for
InGaAsP LED structures [15,16]. The indication of all this data is that the
reliability of InGaAsP lasers and LEDs is potentially as good as that observed
for GaAs/AlGaAs devices.

15. G. H. Olsen, C. J. Nuese, and M. Ettenberg, J. Quantum Electron. QE-15,
     688 (1979).
16. R. L. Hartman and R. W. Dixon, Appl. Phys. Lett. 26, 239 (1975).

TABLE 6. ADDITIONAL OUTPUT POWER VS INPUT CURRENT DATA FOR VPE LEDs

Diode #	Stripe	$I_f = 100$ mA dc P_{mW}	$I_f = 200$ mA dc P_{mW}
2B		0.651	1.179
1B(2)	10xST	0.314	0.463
2B(2)	10xST	0.310	0.437
1C	5xST	0.280	0.325
3C	5xST	0.260	0.316
4C	5xST	0.290	0.353
1D	12xST	0.235	0.474
2D	12xST	0.348	0.555
3D	12xST	0.345	0.498
4D	12xST	0.325	0.510
5D	12xST	0.220	0.289
1E	4xST		
2E	4xST	0.330	0.361
3E	4xST	0.340	0.217
1F	6xST	0.235	0.315
2F	6xST	0.270	0.348
4F	6xST	0.780	0.210
5F	6xST	0.255	0.330
6F	6xST	0.290	0.363
7F	6xST	0.275	0.341
8F	6xST	0.228	0.350
1G	10xST	0.372	0.523
2G	10xST	0.342	0.527
3G	10xST	0.388	0.564
4G	10xST	0.329	0.457
1H	7xST	0.318	0.450
2H	7xST	0.425	0.590
3H	7xST	0.301	0.403
4H	7xST	0.448	0.622
5H	7xST	0.293	0.395
6H	7xST	0.425	0.586
1J	10xST	0.216	0.313
2J	10xST	0.103	0.140
3J	10xST	0.155	0.229
4J	10xST	0.160	0.239
5J	10xST	0.153	0.223
6J	10xST	0.090	0.139
7J	10xST	0.235	0.291
8J	10xST	0.165	0.251
9J	10xST	0.219	0.333
10J	10xST	0.184	0.267
11J	10xST	0.195	0.270
12J	10xST	0.265	0.352
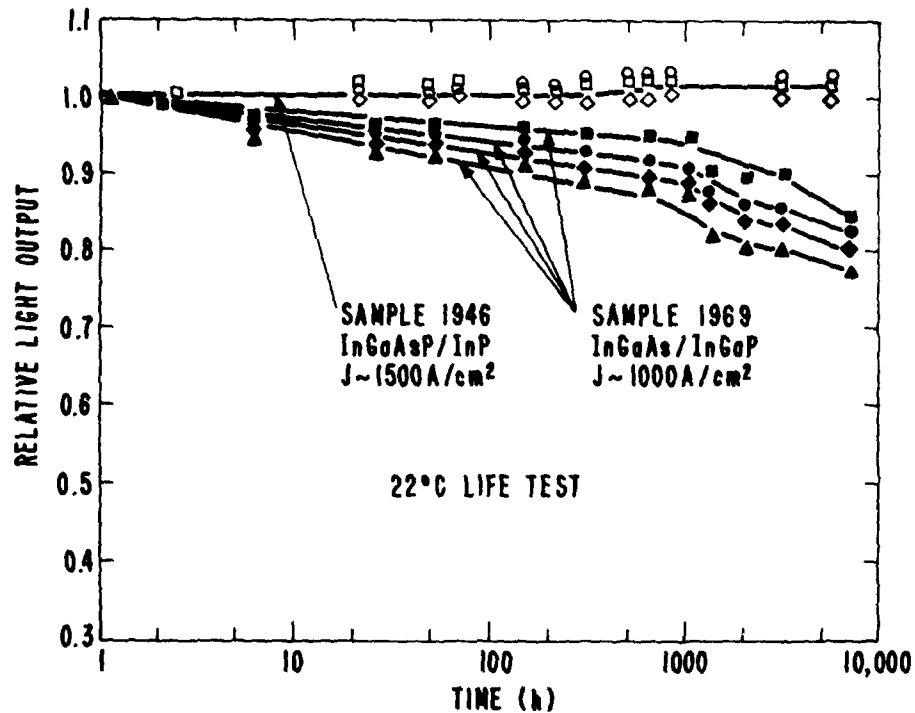
Figure 31. Relative light output vs time at room temperature for InGaAsP/InP quaternary and InGaAs/InGaP ternary LEDs.
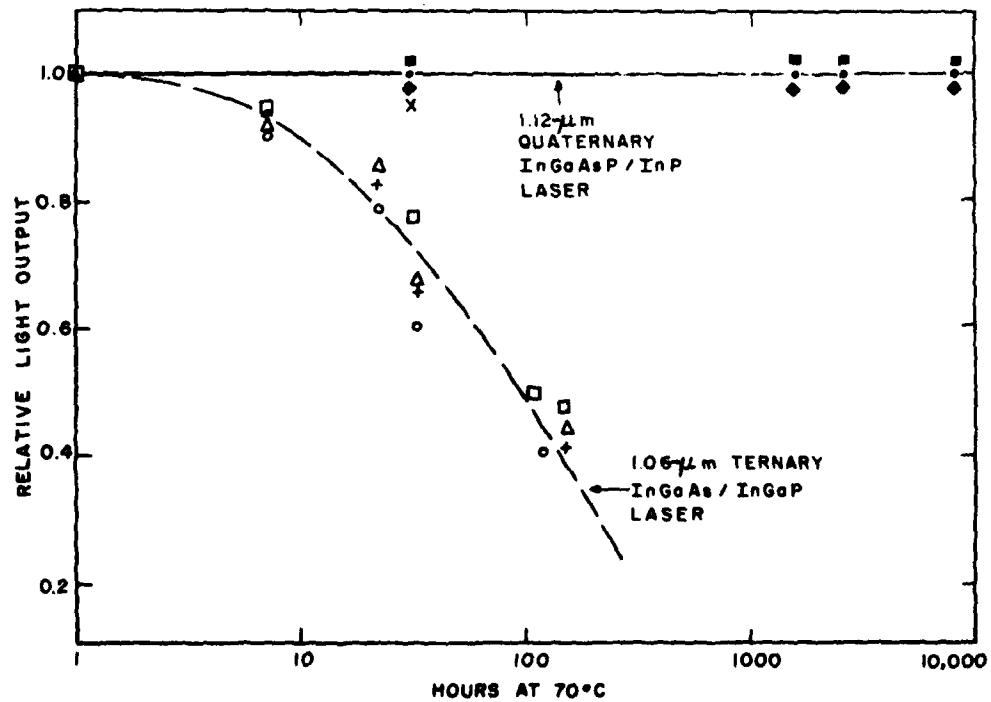
Figure 32. Relative light output vs time at 70°C for InGaAsP/InP quaternary and InGaAs/InGaP ternary LEDs.

43

XII. CONCLUSIONS

1.   1.06-μm VPE LEDs can be fabricated with power efficiencies near 0.45% and halfwidths of ~500 Å.

2.   1.27-μm InGaAsP/InP LED structures can be synthesized via both LPE and VPE (η ~0.6%) with spectral halfwidths of 700 to 750 Å.

3.   Over 100 μW of optical power (~10% coupling efficiency) could be coupled from a VPE edge emitter into a 50-μm core graded index 0.2-NA fiber.

4.   Surface-emitting LEDs can be made from both LPE (η~1.6%) and VPE (η~1%) InGaAsP/InP structures. These devices both have spectral halfwidths of ~1300 Å. However, we feel that our structure is not yet optimized for best coupling into optical fibers.

5.   Typical pulse fall times and modulation bandwidths measured were:

	Fall time (ns)	Bandwidth (MHz)
VPE edge	8	100
LPE edge	9	80
VPE surface	10	75
LPE surface	12	60

6.   Good wafer-to-wafer LED device reproducibility was obtained from both LPE and VPE material.

7.   Experiments with AlGaAs/GaAs devices have shown that for most high-speed (>20 Mbits) fiber-optic applications, edge-emitting LEDs are superior to surface-emitting LEDs.

8.   Initial lifetest shows that VPE-grown edge-emitting LEDs are potentially very reliable with little degradation exhibited for >10,000 h of operation at room temperature and >9,000 h at 70°C.

REFERENCES

1. N. Horiguchi, Electron. Lett. 12, 310 (1976).

2. D. N. Tayne and W. A. Gambling, Electron. Lett. 11, 176 (1975).

3. C. J. Nuese and G. H. Olsen, Appl. Phys. Lett. 26, 528 (1975).

4. J. J. Tietjen and J. A. Amick, J. Electrochem. Soc. 113, 724 (1966).

5. G. H. Olsen and M. Ettenberg, Crystal Growth: Theory and Techniques edited by C. Goodman (Plenum, New York, 1978) Vol. II.

6. H. Nelson, RCA Rev. 24, 603 (1963).

7. H. F. Lockwood and M. Ettenberg, U.S. Patent No. 3 741 825 (1973).

8. C. J. Nuese, G. H. Olsen, M. Ettenberg, J. J. Gannon, and T. J. Zamerowski Appl. Phys. Lett. 29, 807 (1976).

9. G. H. Olsen, C. J. Nuese, and M. Ettenberg, Appl. Phys. Lett. 34, 252 (1979).

10. D. Marcuse, IEEE J. Quantum Electron. QE-13, 819 (1977).

11. D. Botez and M. Ettenberg (J. Quantum Electron. QE-15, 1230 (1979).

12. J. C. Dyment, F. P. Hapron, and A. J. Springthorpe, IEEE Trans. Electron Devices ED-24, 995 (1977).

13. C. A. Burrus and B. I. Miller, Opt. Commun. 4, 307 (1971).

14. H. Kressel, M. Ettenberg, and I. Ladany, Appl. Phys. Lett. 32, 305 (1978).

15. G. H. Olsen, C. J. Nuese, and M. Ettenberg (J. Quantum Electron. QE-15, 688 (1979).

16. R. L. Hartman and R. W. Dixon, Appl. Phys. Lett. 26, 239 (1975).

Comparison of Surface- and Edge-Emitting LED's for Use in Fiber-Optical Communications

DAN BOTEZ, MEMBER, IEEE, AND MICHAEL ETTENBERG, SENIOR MEMBER, IEEE

Abstract—The performance of state-of-the-art double-heterojunction (DH) surface and edge emitters are compared with respect to their use in high-data-rate fiber-optical communication systems. Thick-window (20–25-μm) surface emitters with 2–2.5-μm thick active layers and emitting up to 15-mW optical power at 300 mA have been fabricated. For edge emitters, we use very-high-radiance-type devices with $\simeq$ 500-Å thick active layers. For these two types of LED's we examine differences in structure and light coupling efficiency to fibers of various numerical apertures (NA). For typically good devices we compare the diodes' output power capabilities, the powers coupled into step- and graded-index fibers of various NA, and their respective frequency response. For the same drive current level, we find that edge emitters couple more power than surface emitters into fibers with NA ≤ 0.3. The edge emitters also have ~ 5 times larger bandwidths. We estimate that an edge emitter can couple 5–6 times more power into low numerical aperture (NA ≤ 0.2) fibers than a surface emitter of the same bandwidth. We conclude that edge emitters are preferred to surface emitters for optical data rates above 20 Mbits/s.

I. INTRODUCTION

HIGH-RADIANCE light-emitting diodes (LED's) have been the subject of intensive research and development for fiber-optical communications, due to their linearity, small temperature sensitivity, and inherently small sensitivity to gradual degradation (compared to injection lasers). As a result of these efforts, two basic types of diodes have emerged: surface-emitting LED's [1] and edge-emitting LED's [2]. We present in this paper a comparison between state-of-the-art surface and edge emitters fabricated in our laboratory. The edge emitters are of the "very-high-radiance" type on which we reported previously [3]. The surface emitters are "thick-window" type diodes whose structure and performance are presented below.

The two types of diodes are first compared from a general point of view; differences in structure, emission angular distribution, and the consequent differences in coupling efficiency to optical fibers. For typically good diodes we compare the optical powers emitted into air, the powers coupled into optical fibers of various numerical apertures (NA), as well
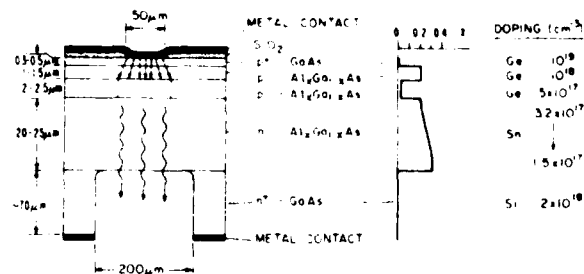
Fig. 1. "Thick-window" DH surface emitter: structure; Al content (x) variation; and doping concentrations.

as their respective frequency response. We find that a surface emitter can couple almost as much power as an edge emitter into low NA fibers, but at a high price in bandwidth. A discussion of the frequency response for the two types of diodes is also presented.

II. THICK-WINDOW (AlGa)As SURFACE EMITTERS

The structure of our surface-emitting LED is shown in Fig. 1. The four-layer double heterojunction (DH) was grown by liquid-phase epitaxy (LPE) between 900 and 840°C in a previously described LPE multibin boat [4]. For most surface emitters the n-(AlGa)As confining layer of the DH structure is also the window for the radiation generated in the active layer. We use the name "thick-window" for our diodes, since the n-AlGaAs layer was grown much thicker than for a regular DH laser structure (i.e., 20-25 μm versus 2-3 μm). The relatively thick window layer is grown by cooling between 900 and 855°C. As a result of Al depletion from the solution, as well as the difference in segregation coefficients between Al and As [5] a graded $Al_xGa_{1-x}As$ layer results with an Al concentration x varying between 0.34 and 0.22 over ~22 μm (see Fig. 1). The thick-window layer provides a sturdy diode base, which in turn considerably eases diode handling and potentially gives a more reliable device. Furthermore, the thickness of the window layer does not seem to affect the diode external efficiency since the light emitted in the active layer (x = 0.05-0.07) is only negligibly absorbed in n-$Al_xGa_{1-x}As$ material with $x > 0.2$ and $n < 1 \times 10^{18}$ cm^{-3}. Abe et al. have reported [6] on a similar thick-window structure, which they fabricate by using a modified LPE boat [7].

The active layer thickness in our structure is in the 2.0-2.5-μm range, which has been shown experimentally [8] as well as predicted theoretically [8], [9] to be optimal for maximum diode external quantum efficiency. The doping concentration in the active layer was chosen to be 5×10^{17} cm^{-3} (Ge) in order to improve the device frequency response without affecting its external quantum efficiency. The doping concentrations of the other layers are a compromise between the requirements of good current confinement [10] and low device series resistance. The difference in Al content between the active layer and the passive layers was kept at relatively small values ($\Delta x \approx 0.17$) since for our relatively thick active layers (i.e., >2 μm) the leakage currents are negligible when normally operating current densities are considered [8]. In turn, the relatively low Al content of the passive p layers insures a low device series resistance [11]. By using a thermally
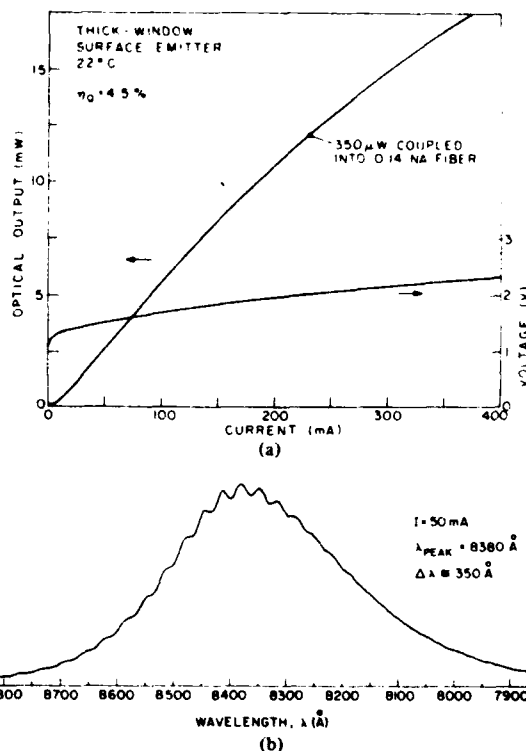
Fig. 2. (a) Output optical power (into air) and voltage drop as a function of dc drive current for the best "thick-window" surface LED (Fig. 1). At the 12-mW output level 350 μW were coupled into flat-ended 0.14 NA step-index fiber of 90-μm-diameter core. (b) Typical spectrum for "thick-window" surface LED's (Fig. 1).

deposited SiO_2 mask and an evaporated metallic trilayer (Ti/Pt/Au), 50-μm-diameter dot contacts were placed on the p side of the wafer. The wells were etched into the n-type GaAs substrate with the mixture $95H_2O_2$ (30 percent): $5NH_4OH$ (29 percent NH_3), which stops at the GaAs-n-$Al_{0.3}Ga_{0.7}As$ interface.

The performance of the best "thick-window" surface emitters thus fabricated is shown in Fig. 2(a) and (b). The output optical power was measured by placing a 1-cm diameter calibrated Si photodiode in close proximity to the etched-well rim of the LED. The output powers at 100 and 300 mA were as high as 5.8 and 15 mW, respectively. Above 200 mA, the power versus current curve deviates from a straight line due to Joule heating. In the linear output regime, an external quantum efficiency as high as 4.5 percent is obtained. These results are comparable to the best results reported in the literature for surface emitters with an active layer dopant concentration in the middle 10^{17} cm^{-3} range [6], [8], [12]-[14]. At the 12-mW output power level, 350 μW were coupled into 0.14 NA flat-ended fiber of 90-μm core diameter (i.e., -15.4-dB coupling loss), without the use of index-matching fluids. Plotted in the same figure is the diode I-V curve, which shows that the device electrical characteristics were quite good (i.e., 1.7-V potential drop at 100 mA and $\simeq$2-Ω series resistance). Fig. 2(b) shows a typical spectrum of our surface emitters. The spectral halfwidth is approximately 350 Å. Many diodes

47

Fig. 3. Surface- and edge-emitting LED's. Top: Schematic representations. Bottom: Isolated active layers with light-generating volumes marked by dashed lines, and the diodes' respective emission angular distributions.
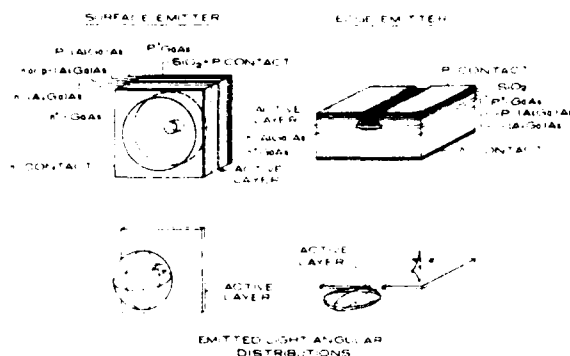
showed interference peaks similar to the ones previously reported by King *et al.* [12] and Shimano *et al.* [15]. These peaks can be represented by the relation

$$\Delta\lambda = \lambda^2/n_{eff}(\lambda)L \qquad (1)$$

where $\Delta\lambda$ is the spacing between the interference peaks, λ is the vacuum wavelength, $n_{eff}(\lambda)$ is an effective index of refraction (which takes into account dispersion effects), and L is the difference in optical path length between the interfering beams. For $\Delta\lambda \cong 34$ Å, $\lambda = 8380$ Å, and $n_{eff} \cong 3.9$ we obtain $L = 53$ μm from (1). This corresponds to interference between transmitted beams and twice-reflected (at the air-window interface and metal-cap interface) beams, in agreement with the findings of Shimano *et al.* [15]. However, our results as well as the ones reported by King *et al.* [12], disprove those authors' assertion that interference peaks cannot occur for active layer thicknesses larger than the electroluminescence wavelength (0.6 μm). Interference patterns should occur as long as the grown layers interfaces are parallel to one another.

III. SURFACE VERSUS EDGE EMITTER: GENERAL CONSIDERATIONS

Fig. 3 displays the geometry and emission distribution for the two types of LED's. For (AlGa)As DH structure surface emitters, a well must be etched through the GaAs substrate to prevent heavy absorption of the emitted radiation. The fabrication also requires precise alignment of the dot contact with the etched well. After etching, the relatively fragile diode base is usually strengthened by electroplating a thick Au layer [12] on the diode p side. By contrast, the edge-emitting LED is fabricated by standard oxide-stripe laser technology without post-contact etching and careful contact alignment. The contact stripes for the edge emitters are 50-70 μm wide, to match typical fiber diameters (50-90 μm). The diodes are usually 100-150 μm long. The front emitting facet has an antireflecting (AR) coating. Similar coatings and/or index-matching epoxies are used in surface emitters for more efficient light extraction [12]. We generally find that the fabrication of
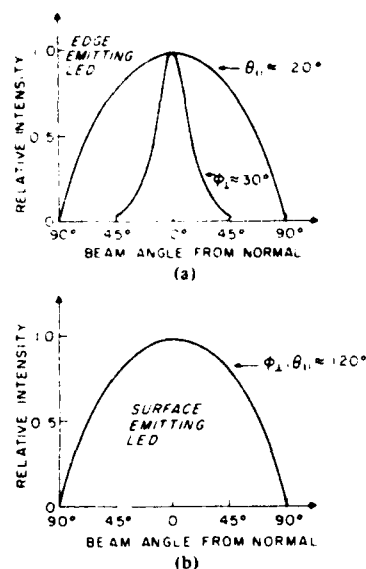

Fig. 4. Typical far-field intensity patterns in the junction plane ($\theta_{||}$) and in a plane perpendicular to the junction ($\phi_\perp$) for: (a) very-high-radiance edge emitters [3]; (b) surface emitters.

surface emitters is more difficult and of much lower yield than that of edge emitters.

The active layers for both types of diodes are shown isolated at the bottom of Fig. 3. The respective light generating volumes for both diodes are indicated with dashed lines. In a surface emitter the generated light spends little time in the active region and thus is not seriously subjected to reabsorption. By contrast, in the edge emitter light must travel most of the diode length before being emitted into the air. As a consequence, edge emitters have lower external quantum efficiencies than surface emitters. However, the effect of absorption in the active layer can be drastically reduced in the edge emitter by making symmetric DH structures of very thin active layers (300-500 Å) [3]. Thus the randomly excited fundamental transverse modes have relatively little overlap of the field intensity with the absorbing active region (as shown in Fig. 3); consequently, the diode external quantum efficiency is increased. The effect can be modeled with the help of the radiation confinement factor Γ_0 [16] applied to a wavelength-averaged background absorption loss coefficient [17].

The most striking difference between the two diodes appears when comparing the angular distributions of their emission. For a surface LED, the emitted light has a two-dimensional Lambertian distribution with a 120° full width at half power (FWHP) beamwidth (Fig. 3 and 4(b)). The corresponding radiation pattern is thus virtually spherical (Fig. 3). For the edge emitter, the presence of a transverse waveguide has the effect of funneling most of the emitted radiation in relatively narrow angles in the plane perpendicular to the junction [20]. As shown in Fig. 4(a) in the plane parallel to the junction the far-field intensity profile is still Lambertian with 120° beam-
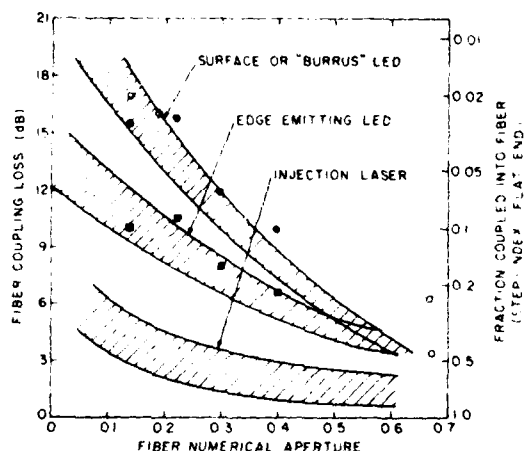
Fig. 5. Relative coupling loss to optical fibers of various numerical apertures for surface emitters, edge emitters, and lasers. The data points are: ● and ■, surface and edge emitters, this work (Fig. 9); ○, surface emitters, from [1], [6], [12].

Fig. 6. Output optical power versus dc drive current for typically good surface and edge emitters. The surface emitters have 50-μm-diameter dot contacts and the edge emitters have 65-μm wide stripe contacts of 100-μm length.

width (FWHP), while in the plane perpendicular to the junction far-field patterns with beamwidths of ~30° can be obtained [3]. The two-dimensional radiation pattern of the edge emitter looks then as an oblate spheroid (Fig. 3). It must be stressed that as opposed to large-optical-cavity-like edge emitters [17], [18], for DH edge emitters the light escaping the active layer gives only a negligible contribution to the device angular distribution [20]. Possible explanations are light absorption in the "cap" layer and substrate and/or spontaneous-emission-rate enhancement for the guided modes [20].

The difference in radiation patterns between surface and edge emitters strongly affects their relative coupling to optical fibers of various NA. Fig. 5 shows the estimated coupling efficiencies for surface emitters, edge emitters, and injection lasers as a function of the NA of flat-ended optical fiber. Coupling efficiency calculations were done for the case when the source size is smaller than the fiber core area. For surface emitters with Lambertian angular distributions the coupling efficiency is simply given by $(NA)^2$ [12], [21]. For edge emitters and lasers one has to numerically compute the coupling integral [21] (i.e., the percentage of the emitted power contained within the fiber acceptance cone angle). The widths of the shaded regions shown in Fig. 5 represent estimated variations in coupling efficiency introduced by several factors: the difference between fiber core and source diameters when the latter is the larger of the two [12]; deviations from a Lambertian angular distribution for the emission of surface emitters; and variations in beamwidth for edge emitters and lasers.

For low NA fibers (i.e., NA < 0.2) the coupling efficiency for edge emitters can be 5 to 7 dB better than for surface emitters (Fig. 5). We also plot experimental data (circles for surface emitters and squares for edge emitters) obtained by us (solid points) or by other workers [1], [6], [12] (open points). As can be seen, the experiments agree reasonably well with the calculated curves. While edge emitters have higher
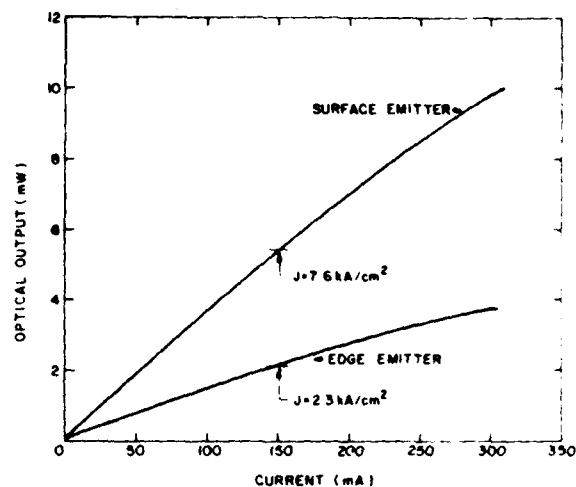
fiber coupling efficiencies than surface emitters it is also true that surface emitters have higher external quantum efficiencies. Thus it is more relevant to compare the absolute coupled optical powers for typically good surface and edge emitters.

IV. SURFACE VERSUS EDGE EMITTERS: TYPICALLY GOOD DEVICES

A. Power-Current Characteristics

Within the same batch and/or from wafer to wafer the fabricated diodes display a certain variation in performance. We find that the scatter in device external efficiency is especially pronounced for surface emitters. We believe that the difference in yield between surface and edge emitters is due on one hand to intrinsically simpler processing to access the generated light in the edge emitter, and on the other hand we find that dot contacts are less adherent than stripe contacts. Lee and Dentai [8] also have reported surface LED efficiency variations (up to 50 percent) for devices from the same batch. The choice of a typically good surface emitter was based on results from a large number of diodes obtained from nine wafers. Specifically, the chosen diode has ~70 percent of the best diode efficiency (Fig. 2(a)), which, as mentioned previously, compares very well with the best results reported in literature [6], [8], [12]-[14] for middle 10^{17} cm^{-3} active region doping levels. We would like to point out that, although lower doping levels (e.g., 10^{16} cm^{-3} and n-type) would provide somewhat higher diode efficiencies [13], such devices would not be relevant for our comparison since their relatively low (electrical) bandwidths (i.e., < 6 MHz) prohibit their use in fiber-optical communications applications [22].

For edge emitters a typically good device was also chosen. The edge-emitting LED's had undoped active layers ≃500 Å thick, spectral halfwidths between 200-250 Å [3], [21], and 100-μm diode lengths. Fig. 6 shows the output power capa-

1234 IEEE TRANSACTIONS ON ELECTRON DEVICES, VOL. ED-26, NO. 8, AUGUST 1979
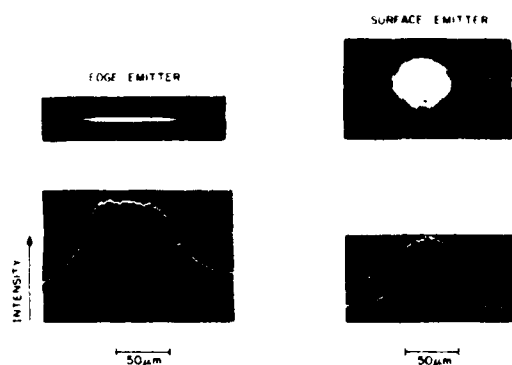

Fig. 7 Near-field photographs (top) and intensity profiles (bottom) for the surface and edge emitter chosen for comparison (Fig. 6)

Fig. 8. Light detected at the end of a 1-km 0.28 NA graded-index fiber (left scale) as a function of the drive current applied to the diodes of Fig. 6. Solid and dashed lines correspond to flat-ended fiber (bottom right inset) and lensed-end fiber (top left inset). The right scale shows the coupled power computed by using the fiber loss coefficient (5 dB/km).

bilities of the two devices. At 150-mA bias the surface LED emits 2.6 times more power than the edge-emitting LED. That occurs, however, at approximately three times more current density for the surface emitter. No index matching epoxies or conformal coatings were used. The near-field photographs and intensity profiles for the two devices are shown in Fig. 7. The surface emitter had a 50-μm contact diameter while the edge emitter had a 65-μm wide contact stripe. In both cases, the emission intensity is quite uniform over most of the emitting region. For coupling to optical fibers both devices were operated at a dc drive current of 150 mA.

B. Coupling to Optical Fibers of Various NA

Both graded- and step-index fibers were used in the coupling experiments. Mode-stripped fibers were placed with the help of a micropositioner inside the etched well of the surface emitters and in close proximity to the air-n-AlGaAs interface. For edge emitters the fibers were positioned close to the diode cleaved facet. The micropositioner was then used to maximize the light coupling. No matching lenses were employed. With one exception (i.e., a lensed 0.28 NA graded-index fiber) all coupling experiments were made with flat-ended (cleaved) fibers.

Fig. 8 shows the results of light coupling to a 1-km-long graded-index fiber of 60-μm core diameter and 0.28 NA. The optical power detected at the end of the 1-km fiber is plotted versus drive current for surface and edge emitters in two cases: flat-ended fiber and lensed-end fiber. The use of a long fiber ensures that the measured power is only that which propagates in the fiber core. Then, by using the fiber loss parameter (5 dB/km in this case) we extrapolate to find the core-coupled powers (right scale in Fig. 8). Over the whole range of drive currents (0-300 mA) the edge emitter is found to couple ≃20 percent more power than the surface emitter. Lensing of the fiber receiving end brings about a 10-percent improvement in coupling efficiency for both LED types. This relatively small difference between the lensed and the flat-ended fibers is most probably due to the fact that the fiber core size is comparable to the size of the sources. Also, due to the radial variation of the refractive index, lensing of a graded-index fiber is less effective in enhancing the coupling efficiency than in the case of a step-index fiber [23].

Fig. 9. Coupled optical powers versus fiber numerical aperture for the LED's of Fig. 6, at the 150-mA drive current level. The photoresponse curves correspond to powers measured as the photodetector was moved at various distances away from the sources. The equivalent NA was calculated by using (2). The data for 0.28 NA graded-index fiber are obtained from Fig. 8.

The difference in emitted power angular distribution between surface and edge emitters is evidenced in Fig. 9 by results of coupling experiments to fibers of various NA, and by photoresponse measurements of a 1-cm-diameter detector at various distances from the two sources. For the latter experiment we calculated the solid cone angle subtended by the detector at a given distance from the source, and translated it into an equivalent NA. The relation used is

$$\theta = \theta_c = \sin^{-1} (NA) \tag{2}$$

where θ is the half-angle of the cone covered by the detector area and θ_c is the fiber critical angle, which from a coupling point of view is the fiber acceptance half-angle. For a step-index fiber $NA = \sqrt{n_1^2 - n_2^2}$ where n_1, n_2 are the refractive indices of the fiber core and cladding, respectively. The photoresponse curves (solid for the edge emitter and dashed for the surface emitter) cross around 0.25 NA, which corresponds to a $14°$ acceptance half-angle. For NA < 0.25 the edge emitter provides more power than the surface emitter into the angle covered by the measurement. The opposite is true for NA > 0.25. These results are supported by light coupling experiments for the two types of diodes to several different NA fibers (round data points for the surface emitter and square data points for the edge emitter). The data points shown in Fig. 9 were obtained for flat-ended step- and graded-index fibers. Specifically, we used 50-μm core diameter step-index fibers of NA values 0.22, 0.28, 0.3, and 0.4; a 90-μm ccre diameter 0.14 NA step-index fiber; and graded-index fibers of 0.14 and 0.28 NA with 90- and 60-μm core diameters, respectively. The fibers were relatively short (3-4 ft) and mode stripped so as to eliminate cladding modes from the measurement. As can be seen from Fig. 9 the surface and edge emitters coupled the same amount of power for NA $\simeq$ 0.3. Just as in the case of the photoresponse curves, for NA values lower than the cross point, the edge emitter couples increasingly better than the surface emitter. Thus for 0.14 NA fibers, the edge LED couples $\simeq$40 percent more power than the surface LED. Similar ratios are obtained when coupling into 0.14 NA graded-index fibers. The coupling efficiencies for these graded-index fibers are about 30 percent of those for step-index fibers of the same NA and core diameter. We conclude that for NA < 0.3 edge emitters couple slightly better than surface emitters and that the roles are reversed for NA > 0.3. The differences, however, are not very dramatic. It will be shown in the next subsection that the real difference between the two emitters lies in their frequency response. We note that our experimentally found crossover point for edge and surface emitters (i.e., NA $\approx$ 0.3) is in good agreement with theoretically calculated values by Gloge [24] (i.e., NA = 0.25) and Marcuse [9] (i.e., NA = 0.23).

C. Frequency Response

The frequency response of the two types of emitters was measured at a bias level of 150 mA and the results are presented in Fig. 10. The measurements were made with a 30-mA peak-to-peak signal. The electrical bandwidth (i.e., the 1.5-dB rolloff point in the modulated light output) is 17 MHz for the surface emitter and 100 MHz for the edge emitter.

To understand this difference, we must explore the factors which control the bandwidth. To first order the electrical bandwidth (f) is a measure of the injected carrier lifetime (τ) [25], [26]

$$f = \frac{1}{2\pi\tau} \tag{3}$$

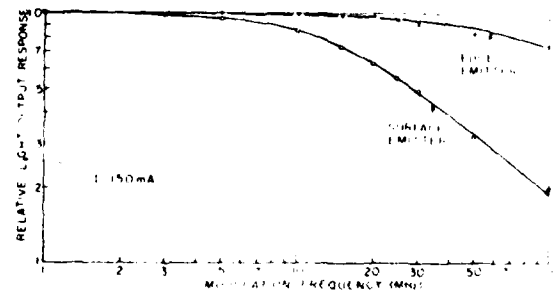which, in turn, is composed of a radiative (τ_r) and a non-

Fig. 10. The frequency response for the LED's of Fig. 6, at the 150-mA drive current level. A 30-mA peak-to-peak signal was used.

radiative (τ_{nr}) part

$$\frac{1}{\tau} = \frac{1}{\tau_r} + \frac{1}{\tau_{nr}}. \tag{4}$$

The nonradiative component for relatively lightly doped active regions and active regions thicknesses (d) less than or equal to a carrier diffusion length is dominated by interfacial recombination velocity (s) at the $Al_{0.22}Ga_{0.78}As/Al_{0.05}Ga_{0.95}As$ interface [27]

$$\frac{1}{\tau_{nr}} = \frac{2s}{d}. \tag{5}$$

The radiative component for a p-type active region is [21]

$$\frac{1}{\tau} = B(p_0 + \Delta n) \tag{6}$$

where B is the recombination coefficient, p_0 is the active region hole concentration, and Δn is the injected carrier concentration.

At injection levels such that the injected carrier density is much lower than the doping density ($\Delta n \ll p_0$) and/or the active region thickness is larger than the carrier diffusion length the lifetime is solely determined by the doping level [8], [21]

$$\frac{1}{\tau} = Bp_0, \qquad \Delta n \ll p_0. \tag{7}$$

At the other extreme, we have the case $\Delta n \gg p_0$ when bimolecular recombination (i.e., direct recombination of injected electrons and holes) occurs and then [21], [28], [29]

$$\frac{1}{\tau} = \left(\frac{BJ}{ed}\right)^{1/2}, \qquad \Delta n \gg p_0. \tag{8}$$

For heavily doped active layers the lifetime is determined (at most current levels) by the doping density level (i.e., (7)). For lightly doped active layers the situation can be quite complicated. Thus as shown by Lee and Dentai for surface emitters [8], as the drive level is increased the lifetime is successively determined by the doping level; by a combination of doping and bimolecular recombination [8], [21]; and by bimolecular recombination (see (8)). For our surface emitters, which are optimized for high external quantum efficiency, the bandwidth is relatively small due to two factors: on one hand we have thick active layers (2-2.5 μm) which considerably reduce
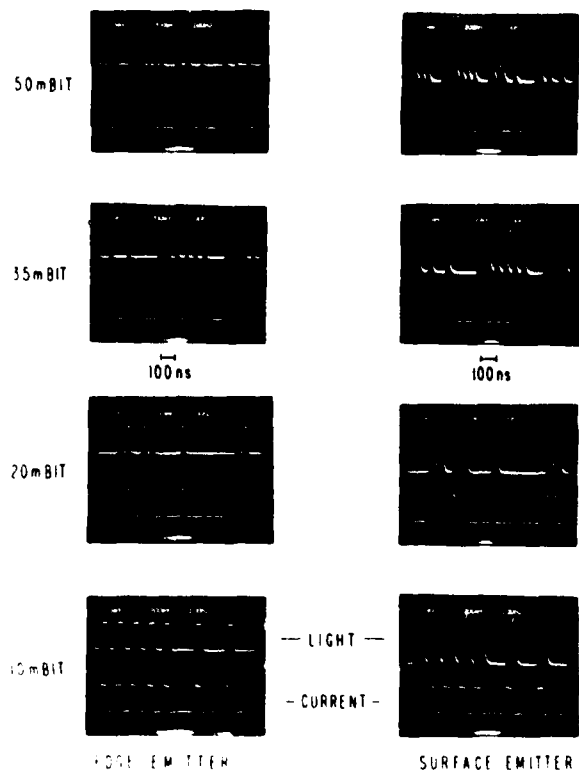
51

50mBIT

35mBIT

20mBIT

10mBIT

— LIGHT —

— CURRENT —

EDGE EMITTER   SURFACE EMITTER

Fig. 11. Optical pulse response of the LED's compared in Figs. 6–10, when subjected to current pulse trains of various data rates.
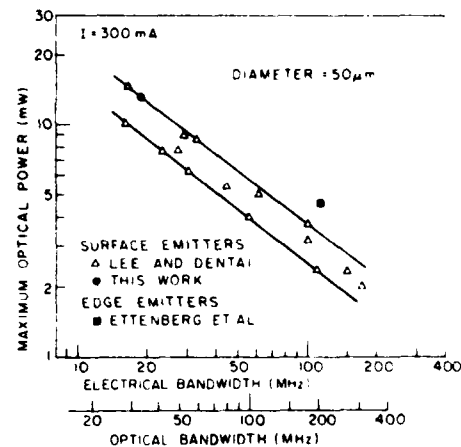

Fig. 12. Output optical power at the 300-mA drive level versus bandwidth for surface emitters reported by Lee and Dentai [8] and for our surface- and edge-emitting LED's. The electrical and optical bandwidths correspond to the -1.5-dB and -3-dB rolloff points in modulated light output, respectively.

the effects of bimolecular recombination (i.e., (8)), and on the other hand, the doping level is moderately low (5×10^{17} cm^{-3}).

The edge emitters studied here (i.e., of undoped and very thin active layers) operate in a regime where the lifetime is controlled almost completely by injected carrier density [3]. Due to strong bimolecular recombination, the edge emitter operates with a short carrier lifetime, which results in a high modulation frequency.

The effect of modulation bandwidth on optical pulse response is illustrated in Fig. 11 for 10-, 20-, 35-, and 50-Mbit/s data rate pulse trains applied to our edge and surface emitters. While the edge emitter can handle each of these data rates comfortably, the surface emitter produces intersymbol interference at rates much in excess of 20 Mbits/s.

For surface emitters, the most common way to increase the bandwidth is to heavily dope the active layer [6], [8], [12] since, as shown in (7), this decreases the carrier lifetime. However, a bandwidth increase by heavy doping occurs at the expense of external quantum efficiency [6], [8], [12], [30]. The decrease in diode external efficiency with increased doping is commonly attributed to an increase in the density of nonradiative recombination centers as the active layer doping density is increased [8], [30], [31]. The tradeoff between P, the output optical power, and f, the electrical bandwidth is best illustrated by the fact that the power–bandwidth product (at the same drive level) is found to be almost constant for all surface emitters of active layer doping concentrations $p_0 > 10^{18}$ cm^{-3} [32]–[35]. For lower doping levels the $P \times f$

product actually decreases with respect to its heavy-doping almost constant value [12], [13]. We show in Fig. 12 output power versus bandwidth results of Lee and Dentai [8] for DH surface emitters at the drive level $I = 300$ mA, and with active layer doping levels in the range 2×10^{17} cm^{-3}–2×10^{19} cm^{-3}. Their data are seen to be bordered by two parallel lines corresponding to $P \sim f^{-0.8}$. Here, it is apparent that the light output of the surface emitter cannot be increased without a corresponding sacrifice in frequency response.

In Fig. 12, we also include our data points for surface and edge emitters versus the results of Lee and Dentai [8]. For the reader's benefit we show a scale of the equivalent optical bandwidth, i.e., the frequency at which the diode light output drops to half its dc value. Our surface emitters (round dot) fall in the range defined by those authors. The edge emitters (square dot) of 120-MHz electrical bandwidth, provide 30–60 percent more power (into air) then surface emitters of same bandwidth. If we now take into account the diodes' respective coupling efficiency to optical fibers (Fig. 5) it becomes obvious that for low NA fibers (i.e., NA < 0.2) the edge emitters couple 5–6 times more power than surface emitters of same bandwidth. Furthermore, this occurs at three times less current density for the edge-emitting LED's.

The question that arises is: can surface emitters be improved to have the same radiance–bandwidth product as that of edge emitters? One approach for increasing the surface LED bandwidth is tight current confinement (e.g., proton bombardment) [13]. Although the bandwidth is increased, the diode external efficiency is reduced and thus the power–bandwidth product is lowered or remains the same as before the current confining process [13]. As in the edge-emitter case, the bandwidth can also be improved by reducing the active layer thickness, since $\tau_r \sim \sqrt{d}$ (see (8)). However, as d is decreased from 2.5 to 0.5 μm, the nonradiative interfacial surface recombination becomes a factor (see (5)), and reduces the diode external quantum efficiency. For instance, the authors of [8] show a reduction in power by as much as a factor of 2 as they decrease

the active layer thickness from 2.5 to 0.5 μm. For layers thinner than 0.5 μm, they find some relative improvement in the diode efficiency, which they attribute to a reduction of the interfacial recombination velocity, in good agreement with the previously reported studies by Ettenberg and Kressel [27]. Thus it is conceivable that surface emitters of very thin active layers ($d \simeq 500$ Å) could achieve higher radiance-bandwidth products than the best surface emitters reported to date.

V. CONCLUSION

State-of-the-art surface-emitting LED's were fabricated and compared to previously reported [3] state-of-the-art edge-emitting LED's. For typically good devices, it is found that at the same drive level, the surface emitter provides 2.5-3 times more power into air than the edge emitter. For evaluation of diode coupling to optical fibers, we used surface emitters with 50-μm-diameter dot contacts and edge emitters with contact stripes 65 μm wide and 100 μm long. Thus at the same drive currents, our edge emitters were operated at a current density approximately 3 times smaller than that of our surface emitters. For fiber NA less than 0.3, edge emitters couple slightly more power than surface emitters (a maximum ratio of 1.4 is obtained for NA = 0.14). For NA > 0.3, the situation is reversed. At the same drive level, the bandwidth of the edge emitter is found to be more than 5 times larger than the surface emitter's (i.e., 100 versus 17 MHz). The power versus bandwidth results are compared to extensive data by previous workers [8]. From that comparison, it is inferred that edge emitters can couple 5-6 times more power in low NA (NA ≲ 0.2) fibers than surface emitters of comparable bandwidth. Based on these observations, we conclude that edge emitters have a clearly superior performance over surface emitters when considering optical communications data rates between 20 and 100 Mbits/s, where low NA fibers are usually required. Surface emitters, in turn, are preferable to edge emitters for short optical data links with high NA fiber [36], [37] and data rates less than 20 Mbits/s. Finally, we find surface emitters to be more difficult to fabricate, and thus potentially more costly than edge emitters.

ACKNOWLEDGMENT

REFERENCES

[1] C. A. Burrus, "Efficient small-area GaAs-Ga$_{1-x}$Al$_x$As heterostructure electroluminescent diodes coupled to optical fibers," *Proc. IEEE*, vol. 59, pp. 1263-1264, Aug. 1971.

[2] M. Ettenberg, K. C. Hudson, and H. F. Lockwood, "High radiance light-emitting diodes," *IEEE J. Quantum Electron.*, vol. QE-9, no. 10, pp. 987-991, Oct. 1973.

[3] M. Ettenberg, H. Kressel, and J. P. Wittke, "Very high radiance edge-emitting LED," *IEEE J. Quantum Electron.*, vol. QE-12, p. 360, 1976.

[4] H. F. Lockwood and M. Ettenberg, "Thin solution multiple layer epitaxy," *J. Cryst. Growth*, vol. 15, pp. 81-83, 1972.

[5] I. Crossley and M. B. Small, "The application of numerical methods to simulate the liquid phase epitaxial growth of Ga$_{1-x}$Al$_x$As from

an unstirred solution," *J. Cryst. Growth*, vol. 15, pp. 268-274, 1972.

[6] M. Abe, I. Umebu, O. Hasegawa, S. Yamakoshi, T. Yamaoka, T. Kotani, H. Okada, and M. Takanashi, "High-efficiency long-lived GaAlAs LED's for fiber-optical communications," *IEEE Trans. Electron. Devices*, vol. ED-24, pp. 990-994, July 1977

[7] S. Isozumi, Y. Komatsu, M. Abe, T. Yamaoka, and T. Kotani, "Liquid phase epitaxial growth of Ga$_{1-x}$Al$_x$As for LEDs with a 50 μm thick window layer," Paper C.1. presented at the 3rd IEEE Specialist Conf. on the Technology of Electroluminescent Diodes, San Francisco, CA, Nov. 1978.

[8] T. P. Lee and A. G. Dentai, "Power and modulation bandwidth of GaAs-AlGaAs high radiance LED's for optical communication systems," *IEEE J. Quantum Electron.*, vol. QE-14, no. 3, pp. 150-159, Mar. 1978.

[9] D. Marcuse, "LED fundamentals: Comparison of front- and edge-emitting diodes," *IEEE J. Quantum Electron.*, vol. QE-13, no. 10, pp. 819-827, Oct. 1977.

[10] J. Zucker and R. B. Lauer, "Optimization and characterization of high radiance (Al, Ga)As double-heterostructure LED's for optical communication systems," *IEEE Trans. Electron. Devices*, vol. ED-25, pp. 193-199, Feb. 1978.

[11] A. J. SpringThorpe, F. D. King, and A. Becke, "Te and Ge Doping studies in Ga$_{1-x}$Al$_x$As," *J. Electron. Mater.*, vol. 4, pp. 101-118, Feb. 1975.

[12] F. D. King, A. J. SpringThorpe, and O. I. Szentesi, "High-power long-lived double heterostructure LED's for optical communications," in *Int. Electron Devices Meeting, Tech. Dig.*, Washington, DC, 1975, paper 21.2, p. 480.

[13] J. C. Dyment, A. J. SpringThorpe, F. D. King, and J. Straus, "Proton bombarded double heterostructure LED's," *J. Electron. Mater.*, vol. 6, no. 2, pp. 173-193, 1977.

[14] J. C. Dyment, F. P. Kapron, and A. J. SpringThorpe, "Top and side emission from double heterostructure LED's and lasers," *IEEE Trans. Electron Devices*, vol. ED-24, pp. 995-1000, July 1977.

[15] N. Shimano, T. Yamamoto, T. Kawasaki, H. Takano, and Y. Morimoto, "Observation of internal interference in emission spectrum of the Burrus type GaAs-GaAlAs DH LED's with thin active layer," *Japan. J. Appl. Phys.*, vol. 17, no. 1, pp. 237-238, 1978.

[16] D. Botez, "Analytical approximation of the radiation confinement factor for the TE$_0$ mode of a double heterojunction laser," *IEEE J. Quantum Electron.*, vol. QE-14, pp. 230-232, Apr. 1978.

[17] D. Botez, P. Zory, and M. J. Brady, "Simple expression for the light output of edge-emitting DH LED's," *Electron. Lett.*, vol. 14, no. 22, pp. 716-718, Oct. 1978.

[18] Y. Horikoshi, Y. Takanashi, and G. Iwane, "High radiance light-emitting diodes," *Japan. J. Appl. Phys.*, vol. 15, pp. 485-492, Mar. 1976.

[19] Y. Seki, "Light extraction efficiency of the LED with guide layers," *Japan. J. Appl. Phys.*, vol. 15, pp. 327-338, Feb. 1976.

[20] J. P. Wittke, "Spontaneous-emission-rate alteration by dielectric and other waveguiding structures," *RCA Rev.*, vol. 36, pp. 655-666, Dec. 1975.

[21] J. P. Wittke, M. Ettenberg, and H. Kressel, "High radiance LED for single-fiber optical links," *RCA Rev.*, vol. 37, pp. 159-183, June 1976.

[22] K. C. Kao and M. E. Collier, "Fiber optical system in future telecommunications networks," *Telecommun.*, p. 25, 1977.

[23] D. Kato, "Light coupling from a stripe-geometry GaAs diode laser into an optical fiber with spherical end," *J. Appl. Phys.*, vol. 44, pp. 2756-2758, June 1973.

[24] D. Gloge, "LED design for fibre systems," *Electron. Lett.*, vol. 13, no. 4, pp. 399-400, July 1977.

[25] Y. S. Liu and D. A. Smith, "The frequency response of an amplitude-Modulated GaAs luminescence diode," *Proc. IEEE* (Lett.), vol. 63, pp. 542-544, Mar. 1975.

[26] H. F. Lockwood, J. P. Wittke, and M. Ettenberg, "LED for high data rate, optical communications," *Optics Commun.*, vol. 16, no. 1, pp. 193-196, Jan. 1976.

[27] M. Ettenberg and H. Kressel, "Interfacial recombination at AlGaAs/GaAs heterojunction structures," *J. Appl. Phys.*, vol. 47, pp. 1538-1544, Apr. 1976.

[28] H. Namizaki, H. Kan, M. Ishii, and A. Ito, "Current dependence of spontaneous lifetimes in GaAs-AlGaAs double heterostructure lasers," *Appl. Phys. Lett.*, vol. 24, pp. 486-487, May 1974.

[29] J. Zucker, R. B. Lauer, and J. Schlafer, "Response time of Ge-

doped (Al, Ga) As-GaAs double-heterostructure LED's," *J. Appl. Phys.*, vol. 47, no. 5, pp. 2082–2084, May 1976.

[30] K. Ikeda, S. Horiuchi, T. Tanaka, and W. Susaki, "Design parameters of frequency response of GaAs-(Ga, Al)As double heterostructure LED's for optical communications," *IEEE Trans. Electron Devices*, vol. ED-24, pp. 1001–1005, July 1977.

[31] T. Yamaoka, M. Abe, and O. Hasegawa, "GaAlAs LED's for fiber-optical communication systems," *Fujitsu Sci. Tech. J.*, vol. 14, no. 1, pp. 133–146, Mar. 1978.

[32] M. Honda, T. Kihara, and M. Endo, "Design and performance of an optical fiber digital link for widespread applications," *Fujitsu Sci. Tech. J.*, vol. 14, no. 3, pp. 1–24, Sept. 1978.

[33] F. D. King, J. Straus, O. I. Szentesi, and A. J. SpringThorpe, "High-radiance long-lived LED's for analogue signalling," *Proc Inst. Elec. Eng.*, vol. 123, no. 6, pp. 619–622, June 1976.

[34] R. C. Goodfellow and A. W. Mabbitt, "Wide-bandwidth high-radiance gallium-arsenide light-emitting diodes for fibre-optic communication," *Electron. Lett.*, vol. 12, no. 2, pp. 50–51, Jan. 1976.

[35] J. Heinen, W. Huber, and W. Harth, "Light emitting diodes with a modulation bandwidth of more than 1 GHz," *Electron. Lett.*, vol. 12, no. 21, p. 553, 1976.

[36] P. B. O'Connor, J. B. MacChesney, and C. M. Melliar-Smith, "Large-core high-N.A. fibres for data-link applications," *Electron Lett.*, vol. 13, no. 7, pp. 170–171, Mar. 1977.

[37] U. Daido, "The estimated coupling efficiency of a light emitting diode with large-core high N.A. fibers," *Fujitsu Sci. Tech. J.*, vol. 14, no. 3, pp. 25–36, Sept. 1978.

54

MISSION

of

Rome Air Development Center

RADC plans and executes research, development, test and selected acquisition programs in support of Command, Control Communications and Intelligence (C^3I) activities. Technical and engineering support within areas of technical competence is provided to ESD Program Offices (POs) and other ESD elements. The principal technical mission areas are communications, electromagnetic guidance and control, surveillance of ground and aerospace objects, intelligence data collection and handling, information system technology, ionospheric propagation, solid state sciences, microwave physics and electronic reliability, maintainability and compatibility.

ATE

LMED

-8